Journal of General Physiology

ARTICLE

Loss of crossbridge inhibition drives pathological cardiac hypertrophy in patients harboring the TPM1 E192K mutation

Lorenzo R. Sewanan[1]*, Jinkyu Park[2,3]*, Michael J. Rynkiewicz[4], Alice W. Racca[5], Nikolaos Papoutsidakis[6], Jonas Schwan[1], Daniel L. Jacoby[6], Jeffrey R. Moore[5], William Lehman[4], Yibing Qyang[2,3,7,8], and Stuart G. Campbell[1,9]

Hypertrophic cardiomyopathy (HCM) is an inherited disorder caused primarily by mutations to thick and thinfilament proteins. Although thin filament mutations are less prevalent than their oft-studied thick filament counterparts, they are frequently associated with severe patient phenotypes and can offer important insight into fundamental disease mechanisms. We have performed a detailed study of tropomyosin (TPM1) E192K, a variant of uncertain significance associated with HCM. Molecular dynamics revealed that E192K results in a more flexible TPM1 molecule, which could affect its ability to regulate crossbridges. In vitro motility assays of regulated actin filaments containing TPM1 E192K showed an overall loss of Ca^{2+} sensitivity. To understand these effects, we used multiscale computational models that suggested a subtle phenotype in which E192K leads to an inability to completely inhibit actin–myosin crossbridge activity at low Ca^{2+}. To assess the physiological impact of the mutation, we generated patient-derived engineered heart tissues expressing E192K. These tissues showed disease features similar to those of the patients, including cellular hypertrophy, hypercontractility, and diastolic dysfunction. We hypothesized that excess residual crossbridge activity could be triggering cellular hypertrophy, even if the overall Ca^{2+} sensitivity was reduced by E192K. To test this hypothesis, the cardiac myosin–specific inhibitor mavacamten was applied to patient-derived engineered heart tissues for 4 d followed by 24 h of washout. Chronic mavacamten treatment abolished contractile differences between control and TPM1 E192K engineered heart tissues and reversed hypertrophy in cardiomyocytes. These results suggest that the TPM1 E192K mutation triggers cardiomyocyte hypertrophy by permitting excess residual crossbridge activity. These studies also provide direct evidence that myosin inhibition by mavacamten can counteract the hypertrophic effects of mutant tropomyosin.

Introduction

Hypertrophic cardiomyopathy (HCM) is an inherited autosomal dominant disorder that results in a host of pathologies at the cell, tissue, and organ level. These include abnormal thickening of the heart wall, cardiomyocyte (CM) remodeling, diastolic dysfunction, myocardial fibrosis, sudden cardiac death, and heart failure (Marian and Braunwald, 2017). HCM is primarily monogenic and caused by mutations in sarcomeric proteins, including thick filament proteins such as myosin and myosin binding protein C, and thin filament proteins, such as tropomyosin, troponins, and actin (Tardiff, 2005).

Recent work using human induced pluripotent stem cell (iPSC)–derived CM (iPSC-CM) models that carry cardiomyopathy mutations have offered the possibility for insight into the early functional impact of these mutations in the context of human cardiac physiology (Eschenhagen and Carrier, 2019). In an elegant study combining genome editing technology with iPSC-CMs, Hinson and colleagues showed that thick filament mutations in myosin and myosin binding protein C manifest a hypercontractile phenotype when examined in engineered heart microtissues (Cohn et al., 2019). Their work, along with other lines of evidence (Mosqueira et al., 2018, 2019; Eschenhagen and Carrier, 2019), establishes mechanical phenotypes as a key aspect of understanding HCM manifestations caused by genetic variants and suggests that such phenotypes are readily apparent in iPSC-CMs, despite some limitations at this early state of iPSC technology (Schwan and Campbell, 2015; Kolanowski et al., 2017).

---

[1]Department of Biomedical Engineering, Yale University, New Haven, CT; [2]Department of Internal Medicine, Section of Cardiovascular Medicine, Yale Cardiovascular Research Center, Yale School of Medicine, New Haven, CT; [3]Yale Stem Cell Center, Yale School of Medicine, New Haven, CT; [4]Department of Physiology and Biophysics, Boston University School of Medicine, Boston, MA; [5]Department of Biological Sciences, University of Massachusetts, Lowell, MA; [6]Department of Internal Medicine, Section of Cardiovascular Medicine, Yale School of Medicine, New Haven, CT; [7]Vascular Biology and Therapeutics Program, Yale University, New Haven, CT; [8]Department of Pathology, Yale University, New Haven, CT; [9]Department of Cellular and Molecular Physiology, Yale School of Medicine, New Haven, CT.

*L.R. Sewanan and J. Park contributed equally to this paper; Correspondence to Stuart G. Campbell: stuart.campbell@yale.edu.

Rockefeller University Press https://doi.org/10.1085/jgp.202012640

Comparatively few iPSC-CM studies have focused on thin filament mutations (Ojala et al., 2016; Wang et al., 2018; Sun et al., 2012; Broughton et al., 2016; Wu et al., 2019), despite clinical evidence demonstrating that thin filament mutations may be associated with a higher burden of left ventricular (LV) dysfunction, heart failure, and, in particular, diastolic dysfunction compared with thick filament mutations (Coppini et al., 2014). In particular, variants in the thin filament protein cardiac tropomyosin (encoded by the gene TPM1) have not been extensively explored using iPSCs or even more traditional approaches, such as animal models (Redwood and Robinson, 2013; Sewanan and Campbell, 2020).

Tropomyosin is a dimeric protein consisting of an α-helical coiled coil. In situ, tropomyosins form a continuous flexible chain along actin to properly regulate activation of the thin filament by calcium (Lehman et al., 2009). Biophysical studies of HCM-associated TPM1 variants indicate that thin filament dysregulation may underlie or initiate cardiac pathophysiology (Redwood and Robinson, 2013; Bai et al., 2013).

In this study, we identified a patient with severe HCM who carries a variant of uncertain significance (VUS) in TPM1, E192K. We used this case to gain novel mechanistic insight into the pathomechanisms of thin filament HCM through a variety of approaches, including engineered heart tissues (EHTs), molecular modeling, and biophysical assays. The results provide a detailed progression of events from altered mechanics of the mutant tropomyosin molecule to the emergence of cellular hypertrophy. We specifically implicate an inability of the thin filament to adequately restrict crossbridge activity as a driver of disease in the case of TPM1 E192K and show that small-molecule inhibition of myosin attenuates disease phenotype.

Materials and methods

Stem cell line derivation

iPSCs were generated from the patient as reported previously (Dash et al., 2016; Seki et al., 2012). Briefly, peripheral blood mononuclear cells were isolated from the blood from patients using Ficoll-Paque PLUS media (GE Healthcare) under Yale institutional review board approval. The collected peripheral blood mononuclear cells were incubated in 1 well of a 12-well plate coated with human anti-CD3 antibody (BD Pharmingen) for 5 d at 37°C. Then, incubated cells were infected with Sendai virus (CytoTune-iPS 2.0 Sendai Reprogramming Kit; Thermo Fisher Scientific). After 24 h, the infected cells were harvested and cultured onto irradiated mouse embryonic fibroblasts (MEFs) with human embryonic stem cell medium (20% knockout serum replacement in Dulbecco's modified Eagle's medium [DMEM]/F12 medium supplemented with 10 ng/ml basic fibroblast growth factor 1% nonessential amino acid [vol/vol], 1% penicillin/streptomycin [vol/vol], 0.1 mM β-mercaptoethanol [Sigma], and 2 mM L-glutamine; Thermo Fisher Scientific). Cells were cultured, and media were changed daily. Multiple colonies appeared around day 30, and multiple clones were established by picking of single colonies. iPSC lines included those of the patient (HCM) and two sex-matched controls (WT1 and WT2) without the patient mutation (Fig. 1 A).

iPSC maintenance and differentiation into iPSC-CMs

iPSCs were cultured in human embryonic stem cell medium (20% knockout serum replacement in DMEM/F12 medium supplemented with 10 ng/ml basic fibroblast growth factor, 1% nonessential amino acid [vol/vol], 1% penicillin/streptomycin [vol/vol], 0.1 mM β-mercaptoethanol [Sigma], and 2 mM L-glutamine; Thermo Fisher Scientific). 70–80%-confluent (4–5-d-old) iPSCs cultured on MEFs were treated with 1 mg/ml dispase (Thermo Fisher Scientific) for 7–9 min. The iPSCs were mechanically dissociated using a 5-ml pipette, collected in a 15-ml Falcon tube, and spun down at 200 rpm for 3 min to deplete the MEF cells. The iPSCs were then plated on a Matrigel (1:60 dilution; Corning)–coated well for culture for 3–4 d in mTeSR medium (05850; STEMCELL Technologies) until ~90% confluency and treated with 20 µM CHIR99021 (Selleckchem) on day 0 for 24 h and 5 µM IWP4 (Stemgent) on day 3 in RPMI/B27 (Gibco) minus insulin media for 48 h. During the cardiac differentiation, we changed the media every other day with RPMI/B27 minus insulin media. After beating, CMs were cultured in regular RPMI/B27 (including insulin) media. CMs at day 14 were treated with 4 mM lactate (Sigma) in glucose-free medium for 4 d to get enriched CMs.

DNA isolation and sequencing

Isolation of genomic DNA from samples was performed using a DNeasy Blood & Tissue Kit (QIAGEN) according to the manufacturer's instructions. DNA samples were amplified using PCR with REDTaq ReadyMix PCR Reaction Mix (Sigma). DNA sequencing was performed by Keck DNA Sequencing Services. Primers are listed in Table 1.

iPSC characterization

For karyotyping analysis (Fig. 1 B), iPSCs were cultured on Matrigel-coated coverslips and underwent G-banding chromosome analysis according to standard procedure by the Yale Cytogenetic Services Core. 10 cells were randomly selected and analyzed. Alkaline phosphatase (AP) staining was performed with an AP Detection Kit (SCR004; Millipore) according to the manufacturer's instructions. For immunocytochemical assay of undifferentiated or differentiated cells, fixed cells with 4% paraformaldehyde/PBS for 12 min were washed with PBS twice and permeabilized with 0.1% Triton X-100 (Thermo Fisher Scientific) for 20 min. After washing with PBS, the cells were incubated with 5% goat serum (Sigma) in PBS for 30 min. Cells were then incubated with primary antibody overnight at 4°C. After washing, the cells were incubated with secondary antibody. Nuclei were stained with 6 ng/ml 4′,6-diamidino-2-phenylindole (Invitrogen). Images were acquired using a Leica DM IRB microscope and captured using Image-Pro Express software. Cell size was measured using ImageJ software after staining with cardiac troponin T (cTnT). Primary antibodies included OCT4 (1:200, ab18976; Abcam), NANOG (1:200, #3580S; Cell Signaling Technology), SSEA4 (1:200, 90231; Millipore), TRA-1-60 (1:200, MAB4360; Chemicon), AFP (1:100, 203A; Cell Marque), desmin (1:200, MAB3430; Millipore), nestin (1:100, ab6142; Abcam), and cTnT (1:500, MS-295-P0; Thermo Fisher Scientific).

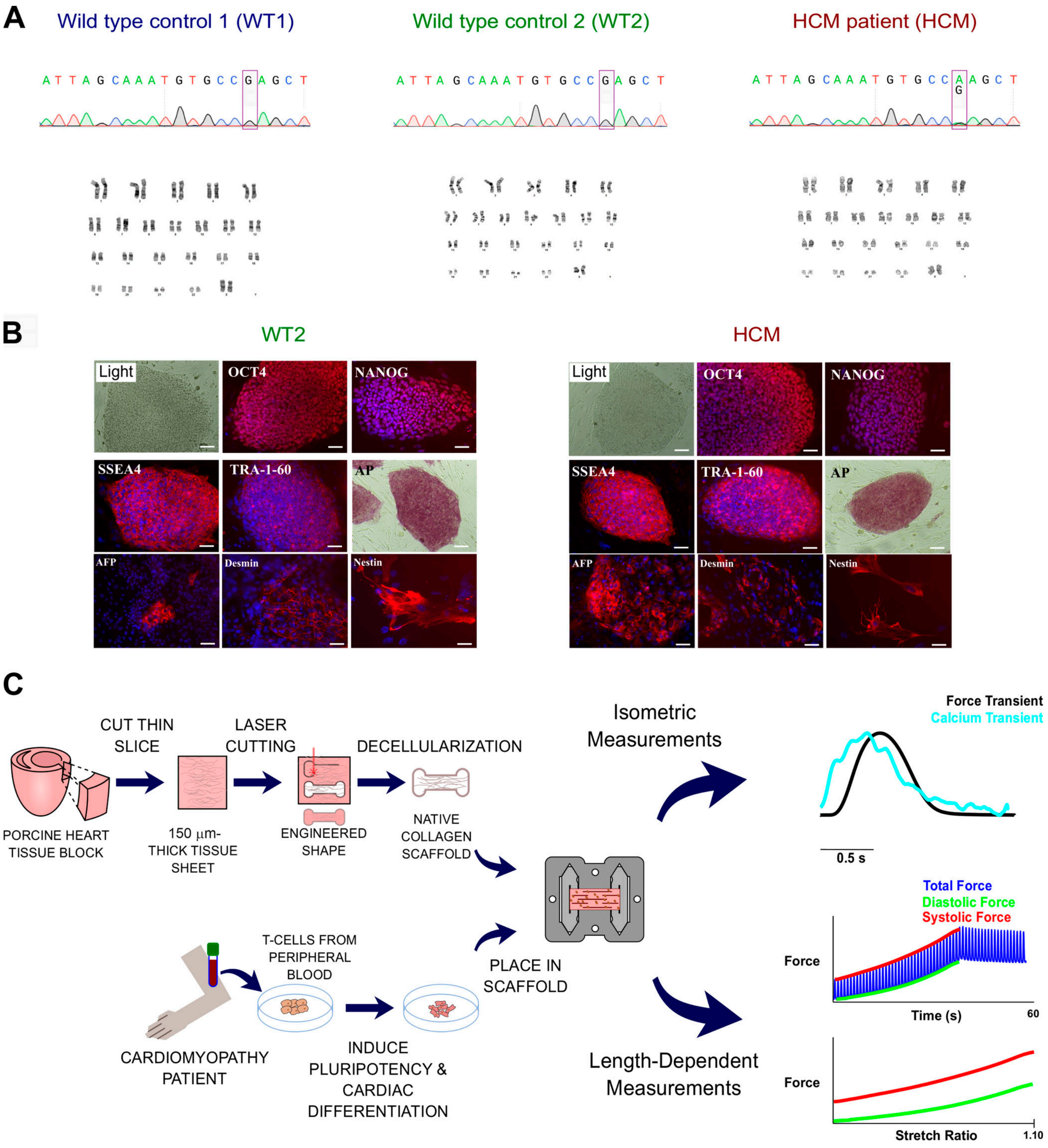

Figure 1. **iPSC and EHT methods. (A)** Three human iPSC lines were used in the study: the HCM patient with the heterozygous c.574G>A (p.E192K) in TPM1 and two WT controls (WT1 and WT2) without any known mutations in sarcomeric genes showing homozygous WT alleles. All iPSC lines showed a normal karyotype. **(B)** WT2 and HCM iPSC lines were originally derived for this work and were tested for markers of pluripotency and differentiation into three lineages. Scale bars, 100 µm. **(C)** EHTs were created from decellularized porcine myocardium seeded with iPSC-CMs. Isometric mechanics, calcium transients, and length–force relationships were measured in EHTs.

EHT fabrication and functional measurements

EHTs made of decellularized myocardium were created similarly to our previously published protocol (Sewanan et al., 2019). Briefly, we cut 150-µm slices from porcine LV blocks, fixed those into our custom tissue culture cassettes (Fig. 1 C), and incubated them overnight in DMEM with 10% FBS and 2% penicillin/streptomycin before seeding them within the next 2 d. iPSC-CMs were dissociated from culture using Accutase treatment

Table 1. **Primers used in the study**

	Description	Product Size (bp)	Forward (5′–3′)	Reverse (5′–3′)
GAPDH	Glyceraldehyde 6-phoshate dehydrogenase	117	GAAGGTGAAGGTCGGAGTCA	TTGAGGTCAATGAAGGGGTC
ANF	Natriuretic peptide A	120	CAGGATGGACAGGATTGGAG	ACAGGAGCCTCTTGCAGTCT
BNP	Natriuretic peptide B	109	TTTGGGAGGAAGATGGACC	TGTGGAATCAGAAGCAGGTG
MYH7	Myosin heavy chain 7	271	ACACCCTGACTAAGGCCAA	AGCTTCTTCTGCAGCTGGC
TPM1	Tropomyosin 1	486	CTACTTTAAGGCAGCCCTTC	CACTGCAATACATTCTCTGC
SeV	Sendai reprogramming vector	181	GGATCACTAGGTGATATCGAGC	ACCAGACAAGAGTTTAAGAGATATGTATC

for 15–20 min followed by washing with PBS and mechanical pipetting. In this study, we seeded either WT1 and HCM or WT2 and HCM cell suspensions at the same time on a prepared batch of scaffolds. We seeded 1 million iPSC-CMs in 50 µl media per scaffold. EHTs were subsequently grown in standard media conditions using RPMI with 2% B27 with insulin for 21 d under electrical field stimulation (2 Hz) to promote maturation (Hirt et al., 2014). Active contraction mechanics were assessed as previously described (Schwan et al., 2016) using a force transducer (WPI KG7; World Precision Instruments) in Tyrode's solution at 36°C. Metrics calculated from the active twitch contractions between 1 and 3 Hz and 100–110% of culture length include peak force (PF), time from stimulus to peak contraction (TTP), time from peak to 50% relaxation (RT50), and normalized tension–time integral (nTTI). nTTI was calculated as the area under the curve of the normalized twitch using numerical integration in MATLAB. To characterize intracellular calcium dynamics, some EHTs were loaded with the ratiometric fluorescent indicator FURA 2/AM (Millipore) by incubation at room temperature for 20 min in loading solution (Tyrode's solution with 17 µg/ml FURA 2/AM, 0.2% Pluronic F-127, and 0.5% Cremophor EL) and subsequently imaged at 36°C using a photometric system as previously described (Schwan et al., 2016). For passive measurements, EHTs were brought to culture length (6.0 mm) on our apparatus at physiological pH (7.3) and temperature (36°C). Culture length is referred to as 0% stretch, as it is the precise length at which the EHT is grown, which is reliably ∼0.15 mm longer than the tissue slack length; the force transducer was also zeroed at culture length. 10% stretch above culture length is used as a comparison stretch because it is typically the length of the maximum systolic force production, i.e., L_{max}. EHTs were preconditioned for three cycles of 10% stretch (0.6 mm) at a rate of 0.015 mm/s (0.25% muscle length/s). We determined that three cycles of preconditioning in this manner would subsequently lead to reproducibility in these mechanical measurements, as it is necessary to normalize the residual stresses in viscoelastic tissues (Humphrey et al., 1990). After preconditioning, EHTs were loaded and unloaded three times in Tyrode's solution under continuous linear stretch at a rate of 0.015 mm/s to 10% stretch. The diastolic force produced was extracted by a custom MATLAB script as previously described (Sewanan et al., 2019), which is the EHT force during diastole at a length >0% stretch. EHT cross-sectional area was determined using optical coherence tomography as previously described (Sewanan et al., 2019).

EHT drug treatments and measurement protocols

Mavacamten (Cayman Chemical) stock was prepared at 20 µM in DMSO. For acute paired testing of EHTs with and without mavacamten, EHTs on the mechanics testing setup (as above) were first tested for isometric twitch and length-dependent properties. Perfusate was then exchanged for Tyrode's solution containing 0.5 µM mavacamten, which was rapidly infused in the course of 4 min to exchange the total bath volume. EHTs were then allowed to equilibrate in solution until steady state was reached and allowed to perfuse for an additional 5 min for a total of 30 min in this drugged solution. Identical isometric twitch and length-dependent protocols were then repeated as done before drug infusion. Notably, acute infusion of DMSO vehicle did not alter EHT properties during this time course (data not shown). For chronic treatment of EHTs with mavacamten, EHTs were grown to 21 d and then subjected to 4 d of media supplemented with 0.5 µM mavacamten or DMSO vehicle, changed every 2 d as is typical. On the fourth day, media were removed, and EHTs were washed twice with media. EHTs were then grown in this drug-free media for 36 h before functional testing was conducted (as above). Preliminary experiments revealed that the inhibitory effect of mavacamten on crossbridges was present for at least 8 h after removal of drug and washing of tissues, therefore necessitating a longer washout period to remove the acute inhibitory effect of the drug.

MD simulation

MD simulations on tropomyosin were performed as previously described (Li et al., 2010a). Briefly, the initial structure comprised the backbone from the Lorenz–Holmes model and side chains oriented using information from crystal structures of tropomyosin fragments as previously described (Rynkiewicz et al., 2015). The mutation of Glu192 to Lys was performed using the Mutator plugin in VMD (Humphrey et al., 1996). All simulations were performed in CHARMM (Brooks et al., 2009) force field version 27 in implicit solvent implementing the Generalized Born with simple switching solvation with previous parameters. Langevin MD simulations were performed with a frictional drag of 1/ps applied to all the surface atoms on tropomyosin (other than hydrogens) with a solvent-accessible surface >1 Å² (solvent probe radius of 1.4 Å). The dynamic integration time step was set to 2 fs with the SHAKE protocol activated for hydrogens. The energy-minimized tropomyosin was heated from 0°K to 300°K for 30 ps, followed by constrained equilibration with gradual release of constraints over 300 ps.

Production runs followed, collecting conformers every 1 ps during a 30-ns simulation time.

Structural modeling of actin–TPM1 interactions

We further used structural models of actin and TPM1 derived from cryo-EM to examine the molecular interactions between actin and specific residues on TPM1, assuming no change in TPM1 binding to actin given that E192K readily assembles into functional thin filaments. Specifically, using flexibility fit models to the cryo-EM densities of thin filaments that have been recently published (Yamada et al., 2020; Doran et al., 2020; Pavadai et al., 2020), we analyzed the actin–TPM1 interactions around residue 192 as it transitions from open to closed to blocked states.

Coarse-grained modeling

To predict the effects of local tropomyosin stiffness on thin filament activation dynamics, we represented just a portion of the flexible tropomyosin cable. The objective was to estimate the bending energy that would result when two adjacent tropomyosins occupy distinct azimuthal positions. Accordingly, we depicted two half-tropomyosin molecules that span actin between two regulatory units (RUs) from troponin I (TnI) to TnI with associated overlap region, including proximal tropomyosin N terminus and distal tropomyosin C terminus. While the molecules were clamped at either end, the freely movable portion of the cable included amino acid residues 6–273 overlapped by 10 residues at the overlap region. To approximate the azimuthal motion of tropomyosin around actin, we assumed that this motion resembles the movement of a guided-clamped flexible beam in a 2-D plane formed by the surface between tropomyosin and actin. Given an approximately symmetric motion of tropomyosin between TnI on either side of the overlap region, we consider deformation of each tropomyosin half-molecule from TnI to overlap, spanning 134 residues plus a 10-residue overlap.

Each tropomyosin half-molecule is considered to be deformed azimuthally to an angle θ as predetermined by known structural positions of tropomyosin on actin with thin filament activation in the three-state model. As a mechanical analogue, each half-tropomyosin was represented as a flexible cable consisting of N links of constant length l connected by torsional springs with individual torsional stiffness β_i. This torsional stiffness was set as the relative stiffness at each amino acid residue along tropomyosin, derived from the MD simulations. The half-tropomyosins were displaced by an orthogonal load F applied at the free end. In each simulation, F was increased until achieving a desired deflection δ from the initial undeformed azimuthal position

$$\delta = 2\pi s \frac{\theta}{360} \frac{1}{2},$$

where θ is the azimuthal position of tropomyosin about actin and s = 40 Å (Orzechowski et al., 2014b).

To compute deformation along the molecule, we consider a vertical tip load F that applies a moment M_i through a virtual moment arm vector A_i on any given torsional spring joint β_i, which must be balanced by its own internal torque τ_i caused by torsional spring rotation ϕ_i, such that

$$|M_i| = |\tau_i|$$
$$|A_i x F_i| = \beta_i \phi_i.$$

We numerically compute the moment exerted by the end load on any given torsional spring joint i with position r_i according to the following equation dependent on the overall chain position R:

$$|M_i| = |R - r_i| * \left[|F|^2 - \left(\frac{F \cdot R^T}{|R - r_i|} \right)^2 \right]^{0.5}.$$

We apply the boundary condition that the proximal end of the chain is fixed and cannot be deformed. As this problem is underconstrained with N degrees of freedom compared with two boundary conditions, we devised an algorithm to iteratively solve this problem by two sequential schemes informed by a semi-inverse approach. First, an optimization problem is performed to adjust the individual angles of the torsional springs of the chain until individual moments are balanced, minimizing these angular residuals as follows within any given instance:

$$\phi_{residual\,i} = \frac{|M_i|}{\beta_i} - \phi_i.$$

The residuals are calculated, and the angles of each individual element are adjusted using a modified gradient descent method with iteration until the maximum angular residual was no greater than a prespecified minimum tolerance threshold, specified as

$$\frac{\alpha}{360} 2\pi,$$

where α was set to 0.1. Next, the overall angular iteration scheme was embedded into an optimization problem to determine a load that would result in a desired total arbitrary azimuthal deformation δ. A numerical solver (*fminsearch*, MATLAB) was used to vary F until the specified tip displacement was achieved.

After the convergence of the model to define a load to meet an azimuthal position θ and the determination of the torsional spring angles achieved to meet that total chain deformation ϕ_i, the energy of the entire chain was calculated as follows:

$$E(\theta) = \frac{1}{2} \sum_i \beta_i \phi_i^2.$$

The chain energy was computed for a variety of θ, ranging from 0° to 35° for the chain, and the calculated energies were fit to determine a global molecule stiffness k using the following equation:

$$E(\theta) = \frac{1}{2} k \theta^2.$$

Relative changes in k for WT and E192K fully reconstructed tropomyosin chains were used to inform the myofilament model parameter identifiable as tropomyosin stiffness γ. Specifically, once k values were obtained for WT and E192K, the ratio of the two was used to scale γ.

Myofilament modeling

Myofilament modeling was performed using a novel extension of our previously published model of thin filament regulation and myofilament activation, with particular emphasis on the structural role of tropomyosin (Sewanan et al., 2016). Previously, the model was only able to accommodate a thin filament of 26 RUs consisting of all WT or all mutant myofilament properties, e.g., a homogenous thin filament. However, the new model allows RUs to be randomly assigned with a probability of being either mutant or WT, allowing the simulation of thin filaments with heterogeneous RU properties, the first model to our knowledge capable of performing explicit heterogenous myofilament simulations.

To develop the model further to allow such heterogeneous thin filament simulations, it was necessary to extend the 6-state Markov Chain–Monte Carlo model as previously described (Sewanan et al., 2016) into a 12-state model, whereby a set of 6 states was created for each type of RU (mutant or WT). Given that the model contains a primary mechanism of RU–RU cooperativity via tropomyosin coupling of any given RU with its neighboring RUs as previously described (Campbell et al., 2010), this necessitated the expansion of the possible transition rates in the transition matrix, depending on the RU properties and the possible neighbor configurations that govern the state transitions from 1,296 terms to 10,368 terms.

The model is governed by eight independent parameters as follows: γ, the tropomyosin chain stiffness; λ, the probability of calcium-independent state transitions; k_{Ca+}, the forward rate for calcium binding to TnC; K_{Ca}, the calcium binding to TnC equilibrium constant; k_{BC}^{ref}, the forward rate for blocked to closed transition; K_{BC}, the blocked-to-closed state transition equilibrium constant; f^{ref}, the forward rate for closed-to-open transition; and δ, the myosin duty cycle. Calculation of transition rates among the various states was done as before, depending on nearest-neighbor states, and linked via tropomyosin stiffness (Sewanan et al., 2016). However, since the filament could now be heterogeneous, we had to consider the cases where a given RU would be linked via tropomyosin to a neighboring RU with properties different from itself. In particular, the juxtaposition of two possible disparate tropomyosins (mutant and WT) was conceived to significantly affect tropomyosin chain dynamics and thereby RU–RU coupling. The effective tropomyosin stiffness between a given RU (Z) and its neighboring RUs (X and Y) determines the effective rate constant, as previously described, according to the following equation for transition to any state (Z^*) described by the rate constant $k_{ZZ^*}^{XY}$:

$$k_{ZZ^*}^{XY} = k_{ZZ^*}^{ref} e^{-\Delta U_Z^X + \Delta U_{ZZ^*}^X - \Delta U_Z^Y + \Delta U_{ZZ^*}^Y}.$$

Tropomyosin contributes to the energy of the transition of an RU Z to a new state Z^* for any given neighbor X (or Y) according to the potential energy ΔU terms. For example, the term describing the potential energy induced by a transition from Z to Z^* given a neighbor X is computed as follows:

$$\Delta U_{ZZ^*}^X = \frac{1}{2}\gamma_{eff}\left(\phi_{ZZ}^* - \phi_x\right)^2.$$

The effective tropomyosin stiffness γ_{eff} depends on the identity of the RU Z and its neighboring RU X. For both RUs being WT, $\gamma_{eff} = \gamma_{WT}$. If both were mutant, $\gamma_{eff} = \gamma_{MUT}$. If one was mutant and one was WT, the effective tropomyosin stiffness was computed as

$$\gamma_{eff} = 2\frac{\gamma_{WT}\ \gamma_{MUT}}{\gamma_{WT} + \gamma_{MUT}}.$$

All other transition rates and potential energies were calculated similarly to the above with substitution of appropriate terms.

Using the transition matrix as described, 24 RUs were used to form a thin filament simulation along with two dummy RUs fixed permanently in the blocked state. Simulations were performed using the Markov Chain–Monte Carlo algorithm as described previously (Sewanan et al., 2016) executed on a NVIDIA Tesla K40 graphics processing card in CUDA C++ with workflows and setups managed through MATLAB. Two main types of simulations were performed for this paper, steady-state activation simulations and twitch simulations. Steady-state activation simulations were used to model the in vitro motility assays and used as input for a variety of a constant calcium concentrations to match those used in the in vitro motility assays. Twitch simulations were used to model the EHT mechanics data and as input for the calcium transient measured in a representative WT EHT. All simulations were started with thin filaments fully deactivated and allowed to simulate for sufficient time and iterations for temporal convergence. Model parameters are listed in Table 2.

Protein preparation for in vitro motility assay

An E192K mutant of WT human-striated α-tropomyosin (Tpm1.1), containing the N-terminal extension Met-Ala-Ser, was obtained from Genewiz using Met-Ala-Ser WT Tpm1.1 template in pET-3D (Orzechowski et al., 2014a). Both WT and E192K plasmids were transformed into Rosetta-competent cells for expression. One liter of cell culture pellet was resuspended in a minimal volume of cold lysis buffer (20 mM Tris, 100 mM NaCl, 2 mM EGTA, 5 mM $MgCl_2$, and protease inhibitors [Pierce Tablets; Thermo Fisher Scientific] at pH 7.5) and lysed by sonication. The insoluble protein and cell debris were then removed by centrifugation. The tropomyosin was then purified following standard methods. Purified tropomyosin aliquots were stored in −80°C until use. Porcine cardiac troponin and actin were prepared from muscle ether powder as described previously (Potter, 1982). Troponin aliquots were stored at −80°C until use; actin was stored at 4°C and used up to 6 mo. Fast chicken skeletal myosin was prepared from freshly slaughtered chicken breast meat following well-established methods (Margossian and Lowey, 1982) and stored in 50% glycerol at 20°C. Lyophilized, purified rabbit skeletal myosin S1 fragments (Cytoskeleton, Inc.) was stored at 4°C until reconstituted in distilled and deionized water, then aliquots were flash frozen in liquid N_2 and stored at −80°C.

In vitro motility assay

Slide preparation solutions were formulated as previously described (Orzechowski et al., 2014a) with some modifications. BSA concentration was increased from 0.5 to 1 mg/ml. For activating solutions, calcium concentrations of in vitro motility

Table 2. **Myofilament model parameters**

Parameter	Description	IVM WT fit	IVM E192K fit	WT twitch fit	E192K twitch
γ ($mol^{-1}kJ$)	Tropomyosin chain stiffness	**33.15**	**23.3**	**42**	**29.4**
λ	Probability of calcium-independent state transitions	0.03	0.03	0.06	0.06
k_{Ca+} ($uM^{-1}ms^{-1}$)	Forward rate for calcium binding to troponin	1	1	0.5	0.5
K_{Ca}	Calcium-binding equilibrium constant	1.4	1.4	1	1
k_{BC}^{ref} (ms^{-1})	Forward rate for blocked-to-closed transition	2.39	2.39	1	1
K_{BC}	Blocked-to-closed state transition equilibrium constant	**7**	**4.2**	**0.9**	**0.54**
f^{ref} (ms^{-1})	Forward rate for closed-to-open transition	0.0999	0.0999	0.2	0.2
δ	Myosin duty cycle	0.17	0.17	0.60	0.60

Bold values are parameters that were altered in the model. IVM, in vitro motility.

solutions were calculated using Ca-EGTA Calculator v1.3. Solutions were formulated using the BATHE_GODT program. Briefly, ~20 µl flow cells were constructed by attaching nitrocellulose-coated coverslips and a standard glass slide with 100-µm-thick 3M double-stick tape. Myosin in myosin buffer was incubated in the flow cell for 1 min. This was followed by 1 cell volume (CV) of 1 mg/ml BSA for 1 min in myosin buffer to remove any unbound myosin and block the remaining surface sites to avoid nonspecific attachment of actin filaments. After blocking, 1 CV of unlabeled actin was added. This actin was allowed to incubate for 2 min before being washed out with 1 CV of actin + ATP buffer and then 4 CV actin buffer to remove the ATP. 1 CV of tetramethylrhodamine-labeled actin filaments in low-salt buffer was then added to the flow cell and allowed to incubate for 2 min. A 1 CV mixture of tropomyosin with/without troponin at equimolar concentrations in far excess of the actin (>600 nM) was added to the cell and allowed to incubate for 6 min. Motility was then initiated by the addition of Ca^{2+}-containing buffers with 1 mM ATP and oxygen scavengers. Movies of actin filament motion on the cover glass surface were captured at up to 5 frames/s on an intensified charge-coupled device camera (Andor iXon) using native camera software. All movies were analyzed using a freeware program designed for the analysis of in vitro motility movies, FAST v1.1 (Aksel et al., 2015). At least six movies of each calcium condition were taken of both WT and E192K tropomyosin. Individual day WT versus E192K data were compared. Data were fit to a standard four-parameter Hill curve.

Quantitative PCR analysis of gene expression

To analyze the gene expression patterns of EHTs generated from iPSC-CMs, total RNA from individual samples was extracted using TRIzol reagent (Invitrogen) according to the manufacturer's instructions. cDNA was synthesized using an iScript cDNA Synthesis Kit (Bio-Rad) according to the manufacturer's instructions. Quantitative PCR amplifications were performed using an IQ SYBR Green Supermix (Bio-Rad) with a total reaction volume of 15 µl containing 1 µl of cDNA, 1.5 µl of primers, and 5 µl of distilled water on a CFX96 Real-Time System (Bio-Rad) under the condition of 95°C for 3 min followed by 46 amplification cycles (95°C for 10 s, 58°C for 10 s, 72°C for 30 s). Glyceraldehyde 3-phosphate dehydrogenase was used as a reference gene for this experiment. Three biological replicates were performed for expression analysis of each gene. Primers used are listed in Table 1.

Western blot for protein quantification

Protein was prepared from iPSC-CMs by direct lysis in ice-cold radioimmunoprecipitation assay buffer containing phosphatase and protease inhibitors (Santa Cruz Biotechnology) followed by collecting of cells using a cell scraper and mechanical trituration. After centrifugation (14,000 *g* at 4°C) for 20 min, the supernatant was collected. Protein content was determine using the Pierce BCA Protein Assay (Thermo Fisher Scientific). Protein was buffered in 4× Laemmli sample buffer (Bio-Rad) and boiled at 100°C for 5 min before electrophoresis. 10 µg of protein were electrophoresed on a 10% Mini-PROTEAN Gel (Bio-Rad) and transferred to a prewetted polyvinylidene fluoride membrane. After blocking and probing with a primary antibody overnight, proteins bands were visualized using an IRDye secondary antibody and visualized using the IR Odyssey imaging system (LI-COR). Total protein loading was further measured for standardization using the REVERT Total Protein Stain Kit (LI-COR). For ERK visualization, rabbit polyclonal phospho-ERK1/2 (T202/Y204, IB 1:500, 9101; Cell Signaling Technology), and mouse monoclonal ERK (clone 3A7, IB 1:500, 9107; Cell Signaling Technology) were used along with LI-COR IRDye 800 goat anti-rabbit (1:10,000) and 680 goat anti-mouse (1:10,000) secondary antibodies.

Statistical analysis

Results are given as the mean with standard error. For a comparison of two groups, statistical significance was determined using *t* test or Mann–Whitney *U* test where applicable, with a confidence level of $P < 0.05$. For paired analysis with repeated measurements on the same samples, paired *t* tests were used with a confidence level of $P < 0.05$. For comparison of groups under multiple conditions, two-way ANOVA was used followed by pairwise comparison using post hoc testing with Tukey correction to determine significant differences, with a confidence level of $P < 0.05$. Statistical analysis was performed using MATLAB and GraphPad Prism 7.

Online supplemental material

Fig. S1 shows cryo-EM modeling of TPM1 traversing over actin. Fig. S2 shows calcium-transient measurements in EHTs made from WT and HCM cell lines. Fig. S3 shows cross-sectional area measurement of EHTs. Fig. S4 shows acute mavacamten treatment of WT EHTs.

Results

HCM patient characteristics

The patient assessed was a 28-yr-old African-American female diagnosed with HCM at age 21 yr. Cardiac magnetic resonance imaging showed asymmetrical hypertrophy with a maximum LV thickness of 30 mm at the basal anteroseptal wall segment (normal, 6–11 mm) together with significant late gadolinium enhancement, consistent with fibrosis, and left atrial dilatation (Fig. 2, A and B). Total LV mass was calculated at 206 g. Echocardiography revealed normal systolic (ejection fraction, 65%) but impaired diastolic function (early transmitral flow velocity with mitral annular velocity [E/A] ratio, 1.2; deceleration time, 126 ms; lateral early diastolic mitral annular velocity [E′], 4.8) with no significant LV outflow tract obstruction (Fig. 2 C). Genetic panel screening at the time of diagnosis revealed a VUS in TPM1, E192K (c.574G>A; Table 3 and Table 4), a variant which has recently been reclassified as likely pathogenic based on genetic testing of more patients reported in ClinVar. No other VUS or pathogenic variants were found in the genes screened. Electrocardiogram showed LV hypertrophy and repolarization abnormalities in multiple leads consistent with HCM (Fig. 2 D).

Family screening revealed that the mother of the patient also had LV hypertrophy, albeit to a lesser degree (17 mm), impaired diastolic function (E/A, 1.4, deceleration time, 160 ms, lateral E′, 8), and a positive test for the TPM1 E192K. These findings were consistent with a diagnosis of familial HCM (Gersh et al., 2011). According to current guidelines, the patient was deemed to be high risk for sudden cardiac death and received an implantable cardioverter defibrillator for primary prevention. In follow-up visits, interrogation of the patient's implantable cardioverter defibrillator revealed short episodes of nonsustained ventricular tachycardia that culminated in an episode of arrhythmogenic syncope 4 yr later. The patient also complained about shortness of breath with minimal exertion (New York Heart Association class III) and frequent episodes of angina, with several visits to the emergency department. The mother of the patient has followed a similar clinical course with limitations in daily function due to severe diastolic dysfunction.

MD and coarse-grained modeling of TPM1 E192K

To examine the molecular underpinnings of the observed clinical phenotypes in patients carrying TPM1 E192K, we performed atomistic MD simulations of WT and E192K tropomyosin. Average structures for E192K compared with WT demonstrated no overt alterations of the coiled coil structure but did show some straightening of the E192K superhelix compared with the WT simulation (Fig. 3 A). Given the important role of tropomyosin's intrinsic stiffness in regulating myofilament activity, we investigated the dynamic persistence length of TPM1. Dynamic persistence length reflects the deviations of tropomyosin from its intrinsically curved structure due to thermal fluctuation and relates to its structural stiffness (Li et al., 2010b). We found that while both WT and E192K experienced significant residue-by-residue variations in flexibility as expected in this α-helical coiled coil, E192K was much more flexible on average (Fig. 3 B).

To predict the effect of the residue-by-residue persistence length differences on the function of the tropomyosin in the context of thin filament regulation, we formulated a novel 2-D coarse-grained model consisting of a series of torsional springs representing each individual residue of TPM1. Each spring was assigned the relative stiffnesses of the TPM1 residues from the MD simulations. The overall chain was deformed by an end load to result in a particular azimuthal displacement, similar to the azimuthal displacements of the tropomyosin molecule across the surface actin during thin filament activation (Fig. 3 C). We conducted numerical experiments displacing the torsional spring chains with either WT or E192K stiffnesses to varying azimuthal displacements (Fig. 3 D) and then computed the total chain energy (Fig. 3 E). We then fit the chain energy (E_B) as a function of the azimuthal displacement (ϕ) according to the torsional spring energy equation

$$E_B = \frac{1}{2}k\phi^2,$$

for both WT and E192K simulations and determined that the global stiffness (k) of tropomyosin with p.E192K was ∼70% that of WT. E192K, therefore, is much more flexible than WT TPM1 at a molecular level, which could have implications for thin filament regulation of crossbridges in the myofilament.

Myofilament modeling and in vitro motility of E192K tropomyosin

After predicting that the stiffness of the mutant E192K tropomyosin varies at a fundamental level from that of WT, we sought to determine how a loss of stiffness might alter the overall function of myofilaments. To do so, we extended our previously published model of thin filament activation (Sewanan et al., 2016) to incorporate the effects of a myofilament composed heterogeneously of WT and mutant tropomyosin RUs to better reflect the heterozygous nature of autosomal dominant HCM. Previously published models allowed only homogenous simulations of either WT or mutant proteins (Land and Niederer, 2015; Sewanan et al., 2016). This new model allows exhaustively random arrangements of heterozygous tropomyosin in the myofilament and is run for all combinations to ensure model convergence.

We used this model to predict Ca^{2+}-dependent sliding velocity (as in the regulated in vitro motility assay) as well as isometric twitch behavior as a function of altered tropomyosin stiffness (Fig. 4 A). A baseline parameter set representing WT tropomyosin behavior was obtained by fitting measurements of mean in vitro thin filament sliding velocity across a range of Ca^{2+} concentrations (Fig. 4 B). Model parameters representing a baseline WT isometric twitch were also obtained by fitting isometric twitch data from a WT human EHT driven by a Ca^{2+} transient measured simultaneously in the same sample (Fig. 4, C

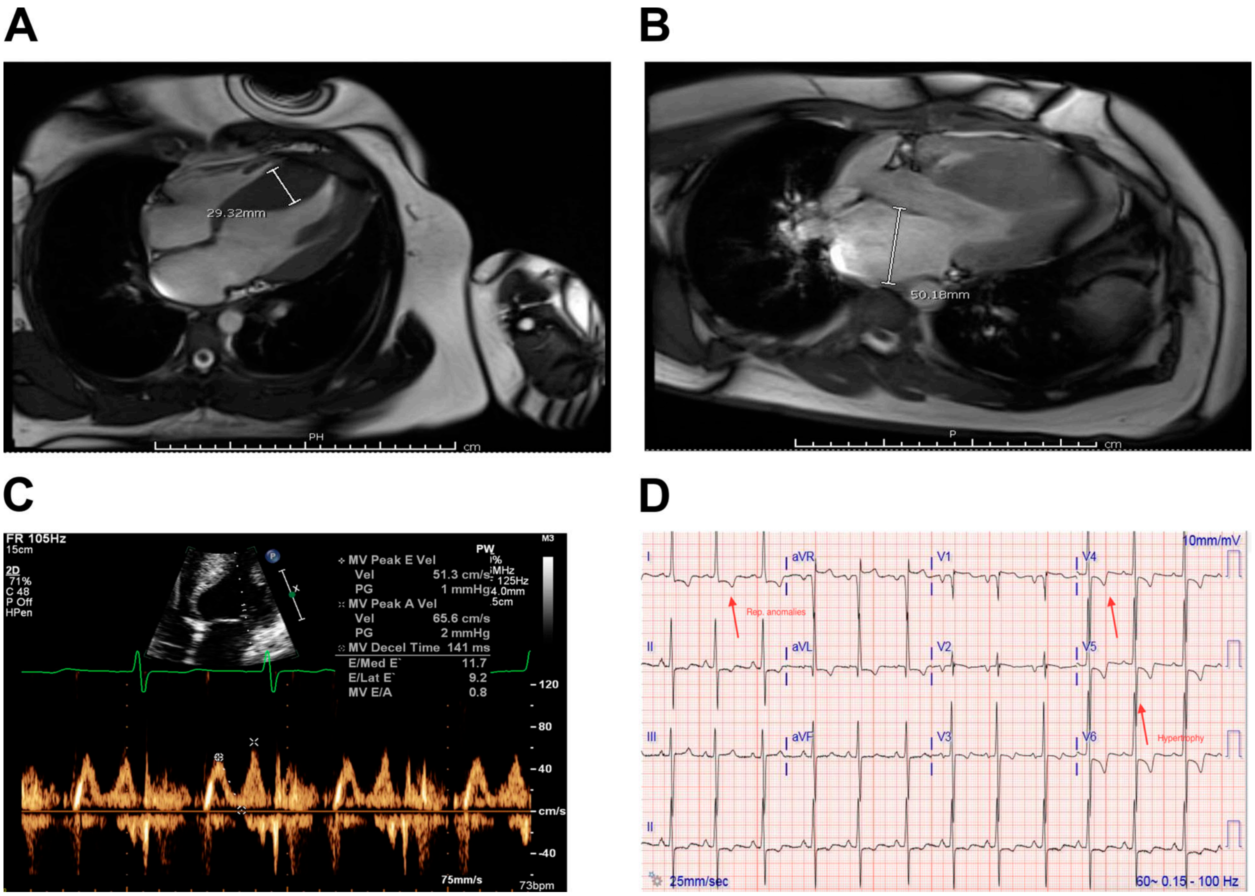

Figure 2. **HCM patient clinical characteristics. (A)** LV end-diastolic wall thickness was ∼30 mm, with a pattern of asymmetric septal hypertrophy. No LV noncompaction cardiomyopathy was observed. **(B)** Three-chamber view on cardiac magnetic resonance imaging. Note significant left atrium enlargement of ∼50 mm. **(C)** Pseudonormal mitral filling pattern on Doppler interrogation with a short mitral deceleration time. Lateral E′ velocity (not shown in this image) was also significantly reduced. **(D)** Electrocardiogram strip showing LV hypertrophy and repolarization abnormalities in multiple leads. This electrocardiogram shows normal sinus rhythm, but the patient is at high risk of developing atrial fibrillation in the future. aVF, augmented vector foot; aVL, augmented vector left; aVR, augmented vector right; MV, mitral valve; PG, peak gradient; PW, pulsed wave; Vel, velocity.

and D). Starting from these WT parameter sets, we then predicted the effects of E192K by reducing tropomyosin stiffness to 70% of that of the WT parameter value. The simulation of regulated in vitro motility predicted elevated velocity at low Ca^{2+} and a loss of cooperativity in response to homozygous expression of E192K (Fig. 4 E). We next used our novel heterogeneous myofilament model incorporating 50% WT and 50% mutant E192K tropomyosin to predict isometric twitch behavior in heterozygous patient myocardium. The mutant simulation exhibited hypercontractility and prolonged twitch kinetics with significantly elevated diastolic force (Fig. 4 F).

In subsequent experiments, regulated in vitro motility characteristics of reconstituted thin filaments containing E192K showed reduced Ca^{2+} sensitivity (Fig. 4 E) in the absence of any differences in maximal sliding velocity (V_{MAX}, measured at 30°C) or cooperativity between WT and E192K-regulated

Table 3. **Bioinformatic characteristics and in silico predictions of TPM1 E192K**

Bioinformatic parameter type	Parameter	Source
Minor allele frequency	0.000000	ExAC (Lek et al., 2016)
No. of HCM cases in OMGL and LMM	13	ACGV (Walsh et al., 2017)
SIFT score (damaging if <0.05)	0.001/damaging	SIFT (Sim et al., 2012)
PolyPhen-2 score (pathogenic if >0.5)	0.013/benign	PolyPhen-2 (Adzhubei et al., 2010)
PROVEAN score (pathogenic if <-2.5)	−2.659/deleterious	PROVEAN (Choi et al., 2012)

ACGV, Atlas of Cardiac Genetic Variation; ExAC, Exome Aggregation Consortium; LMM, Laboratory of Molecular Medicine; OMGL, Oxford Molecular Genetics Laboratory; PolyPhen-2, Polymorphism Phenotyping v2; PROVEAN, Protein Variation Effect Analyzer; SIFT, Sorting Intolerant From Tolerant.

Table 4. **Conservation of TPM1 and TPM1 orthologs for residue E192**

Species	RefSeq accession no.	Protein residues 180–200 (E192 bolded)
Homo sapiens	NP_001018004.1	EERAELSEGKCA**E**LEEELKTV
Pan troglodytes	XP_001173556.2	EERAELSEGKCA**E**LEEELKTV
Macaca mulatta	XP_001104296.1	EERAELSEGKCA**E**LEEELKTV
Bos taurus	NP_001013608.1	EERAELSEGKCA**E**LEEELKTV
Gallus gallus	NP_990732.1	EERAELSESQVR**Q**LEEQLRIM
Danio rerio	NP_001002119.1	EERAEVAEAKSG**D**LEEELKNV
Drosophila	NP_732001.3	EERAEQGENKIV**E**LEEELRVV
Anopheles gambiae	XP_003435938.1	EERAEAGEAKIV**E**LEEELRVV
Caenorhabditis elegans	NP_001021695.1	EERAEAGENKIV**E**LEEELRVV

filaments. Ca^{2+} sensitivity was reduced by ∼0.4 calcium concentration (pCa) units. Since these effects did not seem to be explained solely by the drop in TPM1 stiffness, we hypothesized that the mutation may also alter dynamic interactions between tropomyosin and actin, as previously found in certain model systems (Orzechowski et al., 2014a). Subsequent simulations confirmed that a 40% decrease in blocked-to-closed tropomyosin transition rate, in addition to the E192K-based reduction in stiffness, was able to fit the experimental data with high fidelity (Fig. 4 G). Indeed, when we looked at structural models of TPM1–actin interactions based on more recent, high-fidelity, cryo-EM densities (Pavadai et al., 2020; Yamada et al., 2020; Doran et al., 2020), we determined that the E192 residue of TPM1 typically is required to traverse over a positive patch on actin formed by actin residues K215 and K238 (Fig. S1). Therefore, mutation of E192 to a positively charged lysine residue creates unfavorable charged TPM1–actin interactions that are predicted to hinder the transition rate from open state to blocked state, especially after the detachment of myosin. Based on these structural data, where isometric twitch predictions were updated using this new set of model parameters incorporating loss of stiffness and slowing of blocked-to-closed transition, E192K was found to slightly prolong duration of twitch while substantially reducing PF (Fig. 4 H). Notably, in both predictions of mutant twitches (with or without inclusion of altered blocked–closed equilibrium), a mild elevation of diastolic crossbridge activity is apparent (Fig. 4 I). Computational and in vitro modeling of E192K suggests overall that the mutation results in thin filament dysregulation in which excess residual crossbridge activity is the central feature. We hypothesized that this dysregulation could cause slowed muscle relaxation and increased diastolic force, reflective of the prominent diastolic dysfunction seen in E192K clinical disease.

Mechanical phenotyping of EHTs made with iPSC-CMs

To corroborate predictions of a contractile phenotype in patient myocardium expressing E192K tropomyosin, we leveraged iPSC technology (Lian et al., 2013) and our previously established tissue engineering techniques (Schwan et al., 2016) to create patient-specific EHT constructs. Two control iPSC lines (WT1 and WT2) were generated from sex-matched control subjects, including one iPSC line previously characterized (Dash et al., 2016). Sanger sequencing of all three lines showed that the TPM1 E192K mutant was only found in the HCM iPSC line (Fig. 1 A). Karyotyping of all three iPSC lines after culture to passages used experimentally demonstrated no chromosomal abnormalities (Fig. 1 B). Both newly generated iPSC lines (WT2 and HCM) were characterized fully for pluripotency and showed expression of pluripotency markers and trilineage differentiation (Fig. 1 B).

Using CMs differentiated from each iPSC line, EHTs were formed and grown for 21 d under electrical field stimulation (constant 2 Hz) in standard culture media and then used for mechanical experiments (Fig. 1 C). All data were obtained with a 1-Hz field stimulus under isometric conditions at a physiological temperature and pH with constant perfusion of Tyrode's solution. We ran two sets of independent experiments from at least three differentiation batches per iPSC line, in which the HCM line and one of the WT lines were individually compared. EHTs created from HCM iPSC-CMs exhibited hypercontractility with delayed relaxation compared with both WT controls (Fig. 5, A–C). In particular, HCM EHTs showed an ∼3.5-fold increase in PF relative to WT1 (Fig. 5 G). Furthermore, HCM EHTs showed delayed kinetics of relaxation, with a 35% increase in RT50 (Fig. 5 E). WT1 and HCM EHTs had similar TTP (Fig. 5 D). Overall, HCM EHTs exhibited an increased TTI normalized by individual PF (nTTI) compared with WT1 (Fig. 5 F). Compared with WT2, HCM EHTs showed an ∼5× increase in PF (Fig. 5 K). HCM EHTs showed a slower RT50 compared with WT2 (Fig. 5 I) and a prolonged TTP (Fig. 5 H). Overall, HCM EHTs exhibited a markedly increased nTTI (Fig. 5 J). There did not appear to be any differences in the calcium handling of EHTs made from WT and HCM iPSC-CMs measured using a standard FURA 2/AM fluorescent dye method (Fig. S2). HCM EHTs were thus able to recapitulate some key features of clinical disease caused by the thin filament variant TPM1 E192K, namely impaired relaxation and hypercontractility.

Attenuation of crossbridge-based diastolic force in HCM EHTs by acute mavacamten treatment

Although differing with respect to PF, both model predictions and EHT measurements evidenced enhanced residual crossbridge activity during diastole as a consequence of E192K tropomyosin. To more comprehensively assess the residual force present in EHTs between twitch contractions (diastole), an acute stretch protocol was performed (Fig. 1 C; Sewanan et al., 2019). When the diastolic force–length relationships of WT2 and HCM EHTs were compared (Fig. 6 A), we found that HCM EHTs had a significantly elevated diastolic force (Fig. 6 B). However, there did not appear to be any difference in the cross-sectional area of WT and HCM EHTs (Fig. S3).

We hypothesized that the increased diastolic force could be partly due to excess residual crossbridge activity during diastole due to thin filament dysregulation. If true, this excess diastolic force would be decreased in response to treatment with a myosin inhibitor. We chose the agent mavacamten for these experiments because of its specificity for β-cardiac myosin (the

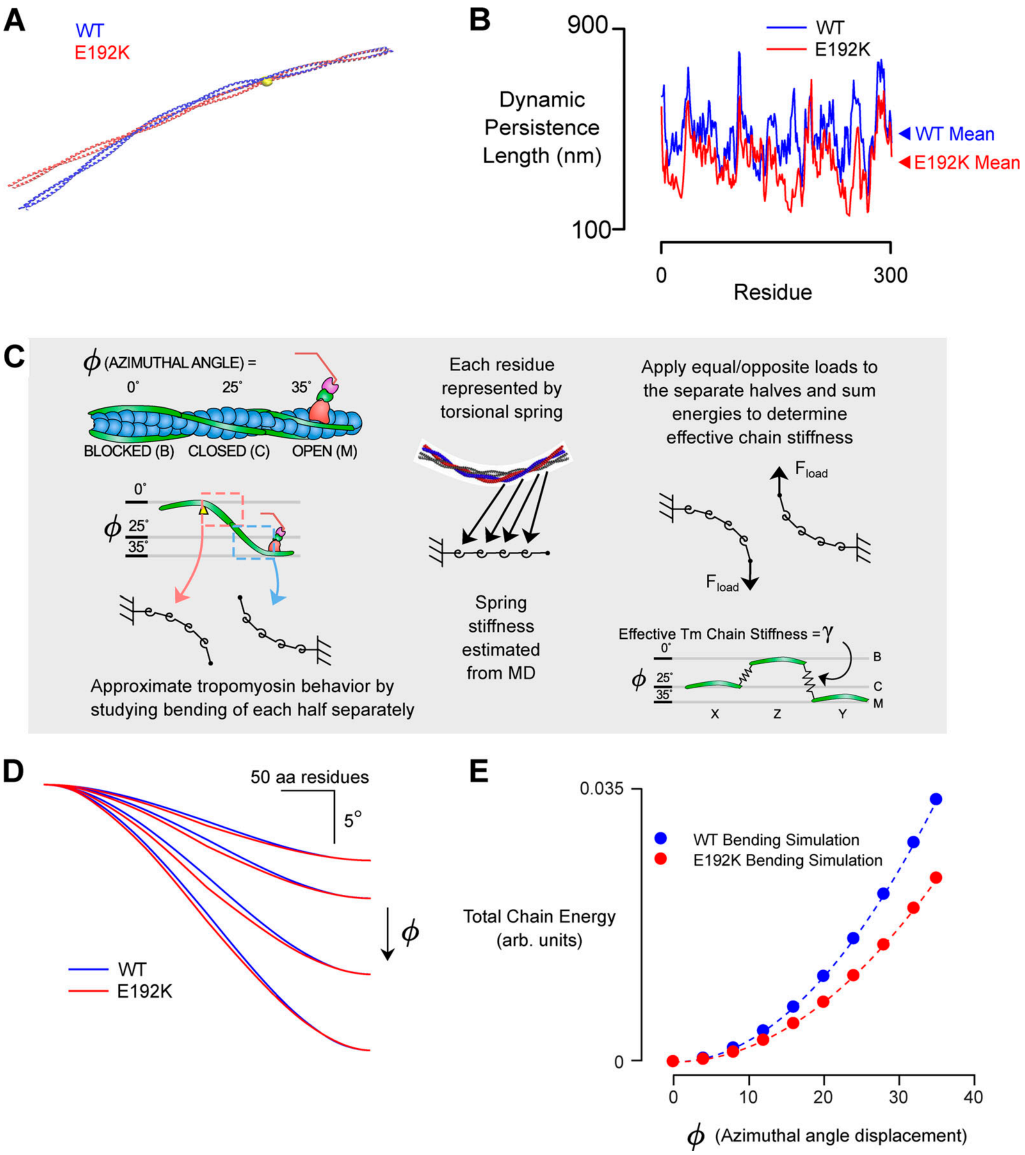

Figure 3. **MD and coarse-grained modeling of TPM1. (A)** Average structures for p.E192K TPM1 compared with WT TPM1 demonstrated no overt structural defects. **(B)** While both WT and p.E192K experienced significant residue by residue variations in flexibility as expected in this α-helical coiled coil, p.E192K was much more flexible on average. **(C)** A novel 2-D coarse-grained model in which a series of torsional springs assigned with the relative stiffnesses of the TPM1 residues could be deformed by an end load to result in a particular azimuthal displacement, similar to the azimuthal displacements of the TPM1 molecule across the surface actin during thin filament activation. **(D)** Simulations displacing the torsional spring chains with either WT or p.E192K stiffnesses to varying azimuthal displacements. **(E)** Total chain energies of WT and p.E192K as a function of azimuthal displacements, with fits overlaid to an elastic energy equation. aa, amino acids; arb., arbitrary; Tm, tropomyosin.

predominant human cardiac isoform and known to be highly expressed in our EHTs; Ng et al., 2020). We subjected HCM EHTs to the stretch protocol before and after an acute 30-min treatment with 0.5 µM mavacamten. This short time frame was chosen because it is the time taken for mavacamten to result in a steady-state effect on contraction and would be too short a time to allow for remodeling of additional components of diastolic force, such as the extracellular matrix (Shen et al., 2021).

As expected, treatment with mavacamten decreased isometric twitch force in HCM EHTs by ~73% (Fig. 6, D and E). Mavacamten acutely reduced isometric twitch force in WT EHTs to a similar extent (~70%; Fig. S4). We have observed similar systolic force reduction under 0.5 µM mavacamten treatment in other studies of WT human EHTs (Sewanan et al., 2021). However, in HCM EHTs, mavacamten also had a significant effect on the diastolic force production (Fig. 6 C). Specifically, mavacamten reduced diastolic force by ~15% compared with paired untreated HCM EHTs after 30 min of treatment (Fig. 6 F). Interestingly, mavacamten also normalized twitch kinetics toward WT values in treated HCM EHTs (Fig. 6, G–I), reducing RT50 by 26% and nTTI by 18% without affecting TTP.

Regression of in vitro hypertrophy by chronic mavacamten treatment

The observation that acute mavacamten treatment reduced diastolic force in HCM EHTs seemed to confirm model predictions

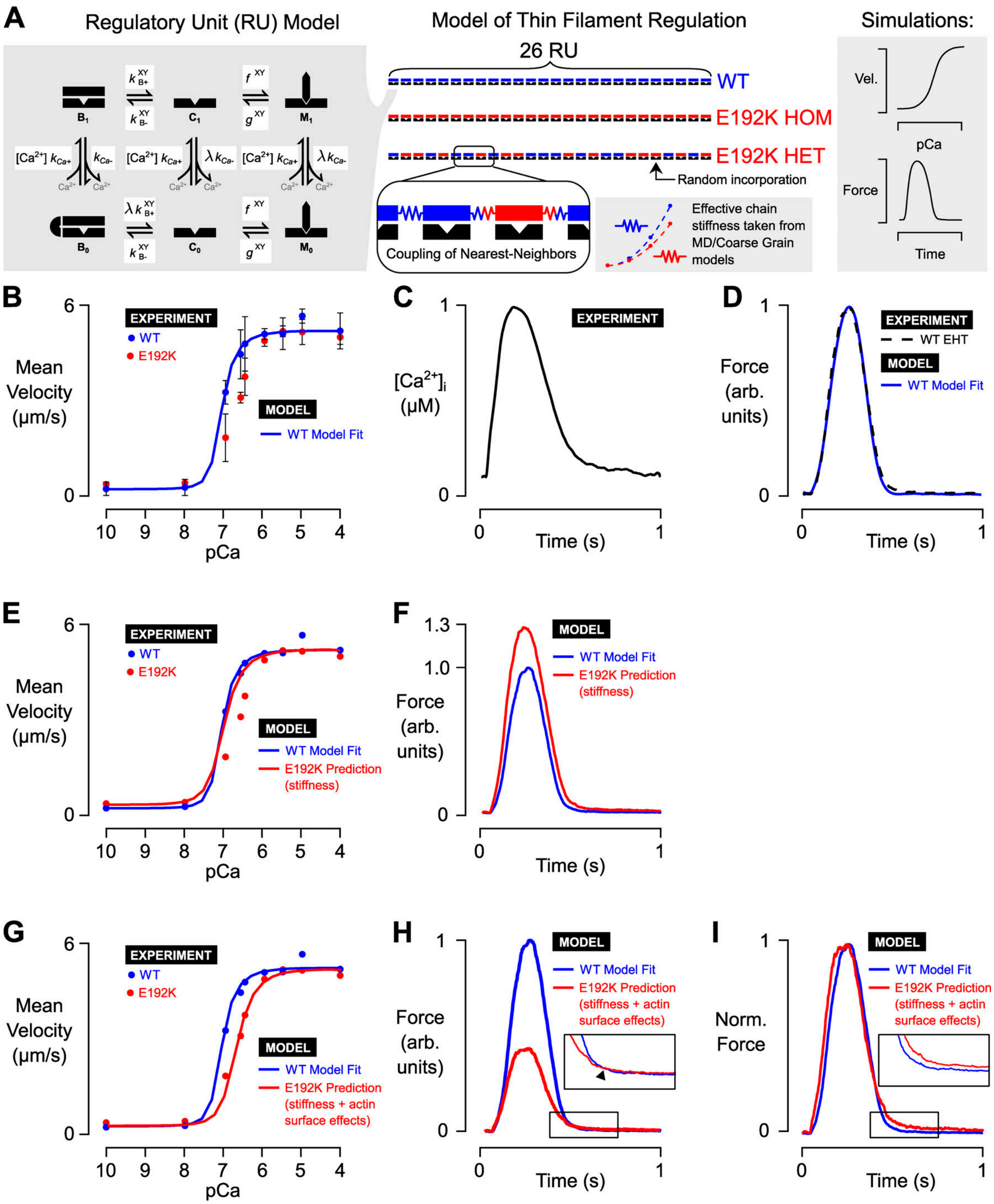

Figure 4. **Stochastic thin filament modeling of TPM1 E192K variant. (A)** Stochastic model of thin filament activation incorporating homozygous (HOM) and heterozygous (HET) myofilament composition with simulations of in vitro motility (IVM) and isometric intact twitch. **(B)** WT IVM data and model fit for determining baseline parameters. **(C)** Calcium transient from WT EHT. **(D)** Isometric twitch from WT EHT and model fit for determining baseline parameters in response to the calcium transient. **(E)** Prediction of p.E192K IVM with decreased stiffness, which does not exhibit decreased calcium sensitivity. **(F)** Predicted twitches for WT1 and p.E192K. **(G)** Fitting of p.E192K IVM with decreased stiffness and decreased blocked-to-closed (BC) equilibrium constant. **(H)** Predicted twitches for WT1 and p.E192K. **(I)** Normalized predicted twitches for WT1 and p.E192K. arb., arbitrary; Norm., normalized; Vel., velocity.

that E192K causes excess residual crossbridge activity during diastole. We next sought to understand why HCM EHTs exhibited dramatic hypercontractility in spite of in vitro motility experiments and modeling that predicted a loss of myofilament Ca^{2+} sensitivity and twitch force in the presence of E192K tropomyosin. We hypothesized that the excess residual crossbridge activity could be leading to cellular hypertrophy in the mutant EHTs, resulting in higher twitch force in spite of any myofilament Ca^{2+} sensitivity changes. We first examined iPSC-CMs grown in standard 2-D culture from WT2 and HCM lines via cTnT immunostaining (Fig. 7 A) to clearly assess cell size. HCM iPSC-CMs had an ~70% increase in cell size (Fig. 7 B). Cellular

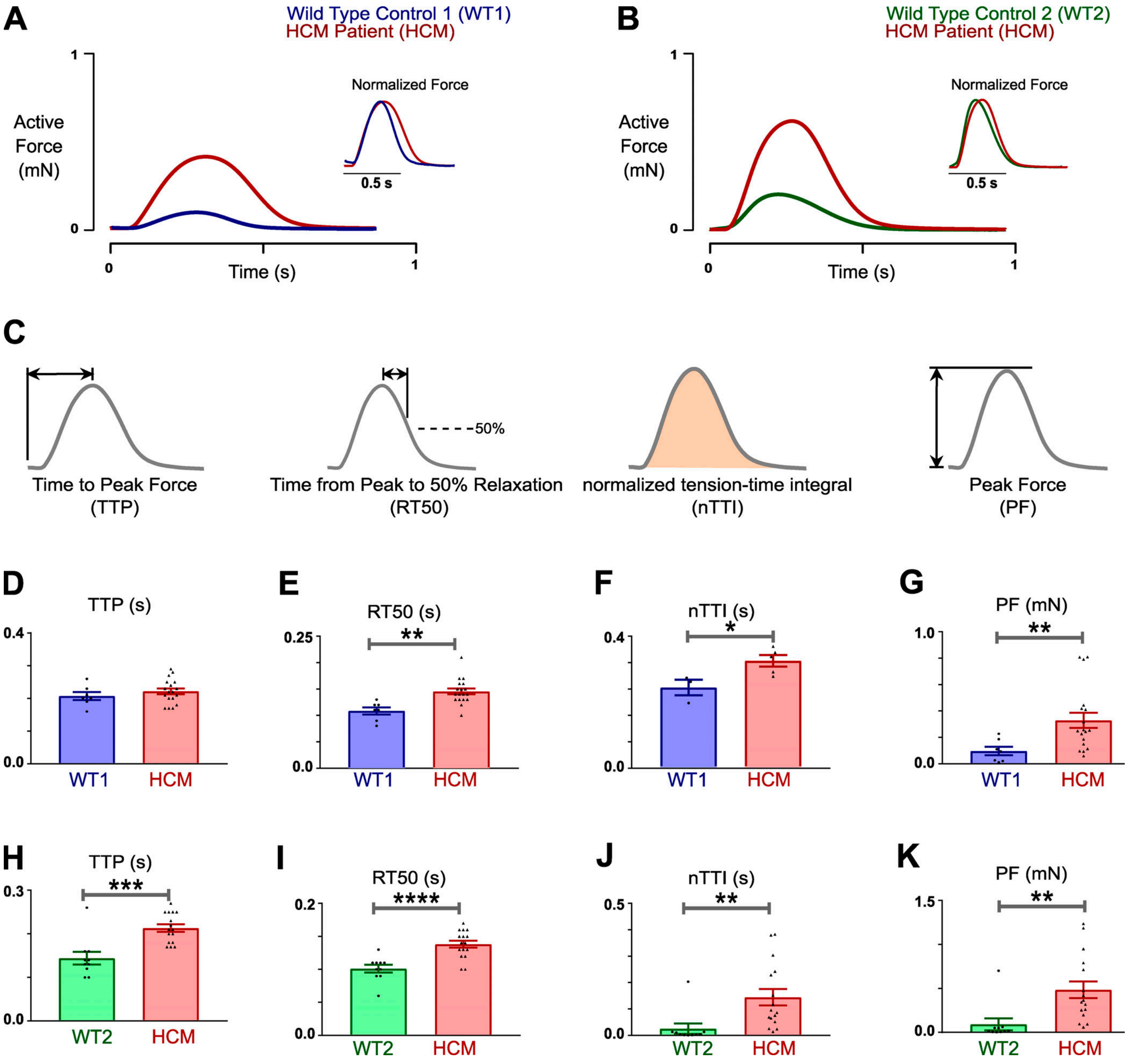

Figure 5. **Mechanics of EHTs created from WT and HCM iPSC-CMs. (A)** Representative EHT twitches from WT1 and HCM. **(B)** Representative EHT twitches from WT2 and HCM. **(C)** Parameters quantified from isometric twitch experiments. **(D)** WT1 and HCM EHTs had similar TTP. **(E)** HCM EHTs showed delayed kinetics of relaxation, with a 35% increase in RT50 (WT1 versus HCM, 0.11 ± 0.01 versus 0.15 ± 0.01 s, P = 0.0012, *t* test). **(F)** HCM EHTs exhibited an increased nTTI compared with WT1 (WT1 versus HCM, 0.22 ± 0.02 versus 0.29 ± 0.02 s, P = 0.03, *t* test). **(G)** HCM EHTs showed an ∼3.5-fold increased in PF (WT1 versus HCM, 0.097 ± 0.03 versus 0.33 ± 0.06 mN, P = 0.0032, Mann–Whitney *U* test). **(H)** HCM EHTs showed a prolonged TTP (WT versus HCM, 0.14 ± 0.015 versus 0.21 ± 0.008 s, P = 0.0002, *t* test). **(I)** HCM EHTs showed a delayed RT50 compared with WT2 (WT versus HCM, 0.11 ± 0.006 versus 0.14 ± 0.005 s, P = 0.0001, *t* test). **(J)** HCM EHTs exhibited a markedly increased nTTI (WT versus HCM, 0.025 ± 0.02 versus 0.15 ± 0.03 s, P = 0.0098, *t* test). **(K)** HCM EHTs showed an ∼5× increase in PF (WT2 versus HCM, 0.091 ± 0.07 versus 0.48 ± 0.10 mN, P = 0.0065, *t* test). Data are mean ± standard error. *, P < 0.05; **, P < 0.01; ***, P < 0.001; ****, P < 0.0001.

hypertrophy in iPSC-CMs was further indicated by the presence of upregulated expression of the hypertrophic marker natriuretic peptide B (BNP; Fig. 7 C) and increased ERK1/2 phosphorylation relative to WT (Fig. 7 D).

Given that mavacamten could reduce excess residual diastolic crossbridge activity as established with acute drug treatment (Fig. 6 F), we hypothesized that chronic treatment with this drug could decrease hypertrophy in HCM EHTs. We subsequently treated HCM EHTs with 0.5 µM mavacamten for 2 d and found that BNP expression was significantly downregulated in HCM EHTs by this chronic mavacamten treatment (Fig. 7 E). EHTs were then treated with mavacamten for 4 d in order to assess whether decreased hypertrophic signaling would correspond with a decrease in EHT contractile force. Critically, in this

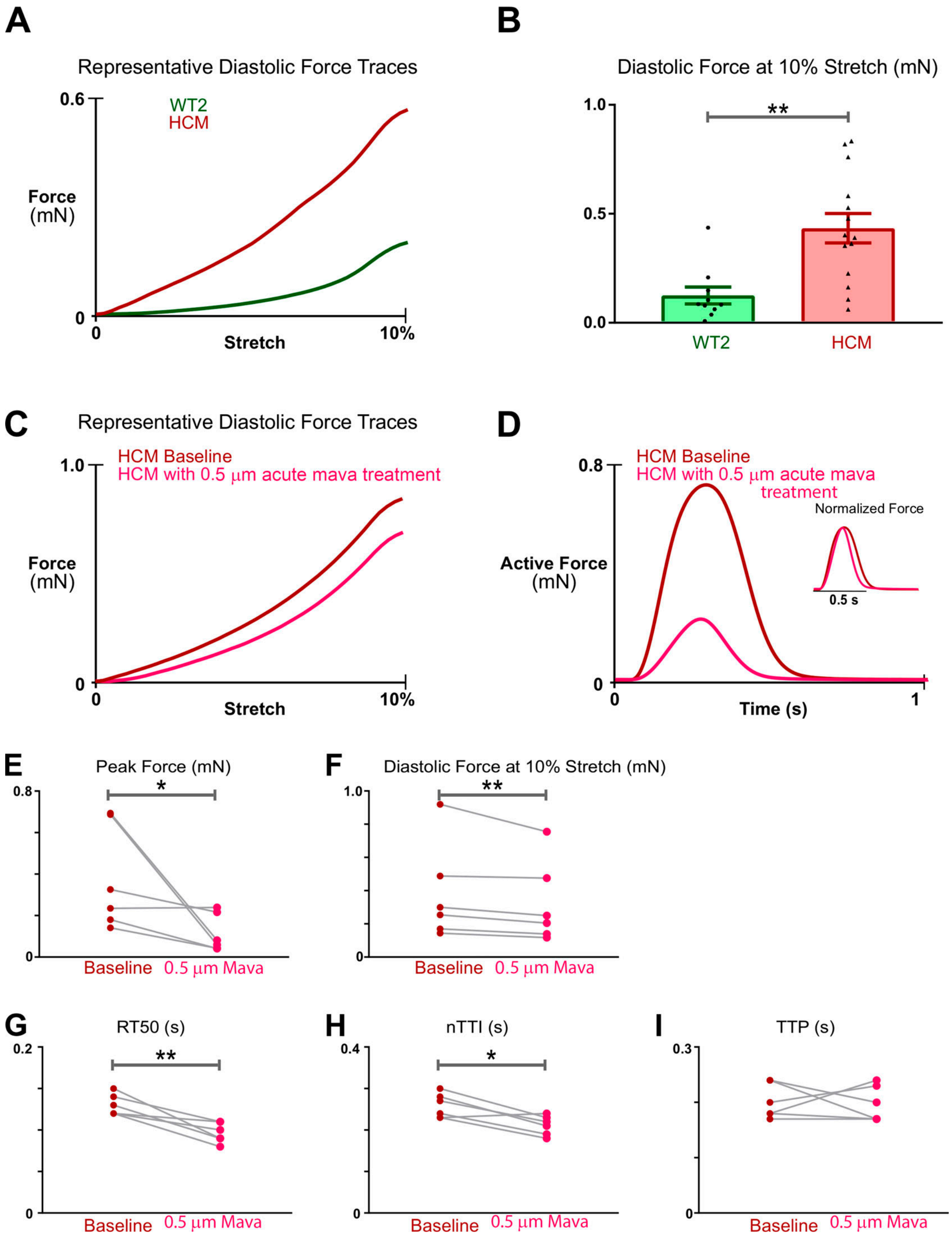

Figure 6. **Diastolic mechanics of EHT and effect of acute mavacamten treatment. (A)** Representative diastolic force–length traces of WT2 and HCM EHTs. **(B)** HCM EHTs had a significantly elevated diastolic force compared with WT2 (WT versus HCM, 0.13 ± 0.04 versus 0.44 ± 0.07 mN, P = 0.002, Mann–Whitney *U* test). **(C)** Representative paired acute measurement of HCM EHT isometric twitch before and after mavacamten. **(D)** Representative paired acute measurement of HCM EHT diastolic force–length relation before and after mavacamten. **(E)** Mavacamten drastically decreased active contractile for production in HCM EHTs, specifically reducing PF by ~73% compared with untreated paired HCM EHTs (P = 0.02, paired ratio *t* test). **(F)** Mavacamten reduced diastolic force by ~15% compared with paired untreated HCM EHTs (P = 0.002, paired ratio *t* test). **(G)** Mavacamten reduced RT50 by 26% (P = 0.006, paired ratio *t* test). **(H)** Mavacamten reduced nTTI by 18% (P = 0.01, paired ratio *t* test). **(I)** Mavacamten had no effect on TTP in HCM EHTs. Data are mean ± standard error. *, P < 0.05; **, P < 0.01. mava, mavacamten.

experiment, EHTs were treated with 24 h of washout following 4 d mavacamten treatment to ensure that only the chronic effects of the drug were observed in the absence of concurrent crossbridge inhibition during testing. In both WT2 and HCM EHTs, chronic mavacamten treatment significantly reduced force (Fig. 7 F). Following chronic treatment with mavacamten, the contractile characteristics of WT2 and mutant EHTs were not statistically different (Fig. 7 F). Furthermore, a significant

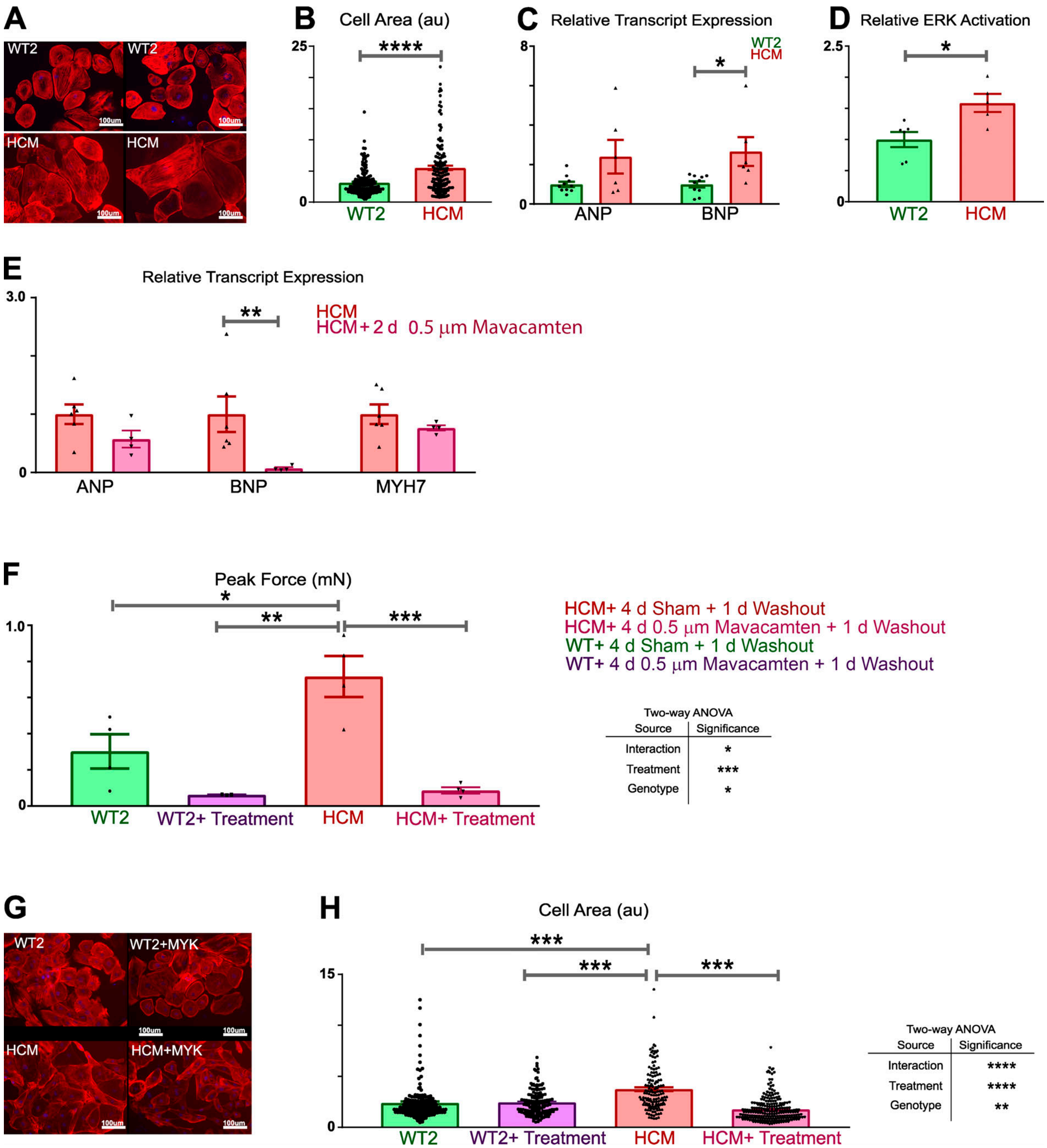

Figure 7. **Chronic treatment of HCM EHTs with mavacamten. (A)** WT2 and HCM iPSC-CM cTnT immunostaining. **(B)** HCM iPSC-CMs had an ~70% increase in cell size ($P < 0.0001$, *t* test). **(C)** BNP was upregulated in HCM iPSC-CMs ($P = 0.0075$, Mann–Whitney *U* test). **(D)** ERK activation was increased in HCM iPSC-CMs ($P = 0.0123$, *t* test). **(E)** BNP expression was significantly downregulated in HCM EHTs by this chronic mavacamten treatment ($P = 0.0095$, Mann–Whitney *U* test). **(F)** Treated and untreated WT2 and HCM EHTs (using two-way ANOVA, interaction $P = 0.03$) in PF was found to be significant, indicating that the chronic effect of mavacamten in decreasing cellular contractile force was greater in HCM EHTs than in WT2 EHTs. **(G)** WT2 and HCM iPSC-CM cTnT immunostaining with and without chronic mavacamten treatment. **(H)** Treated and untreated WT2 and HCM iPSC-CMs (using two-way ANOVA, interaction $P < 0.0001$) in cell size was found to be significant. Data are mean ± standard error. *, $P < 0.05$; **, $P < 0.01$; ***, $P < 0.001$; ****, $P < 0.0001$. ANP, natriuretic peptide A; au, arbitrary units.

interaction was observed between peak isometric twitch force measurements in treated and untreated WT2 and HCM EHTs (two-way ANOVA). This indicated that the chronic effect of mavacamten in decreasing cellular contractile force was greater in HCM EHTs than in WT2 EHTs. We hypothesized that this decrease in HCM EHT contractile force was due to decreased myofibrillar content (atrophy) and next looked at whether we would see this reflected in cTnT imaging of iPSC-CMs. Chronic treatment of WT and HCM iPSC-CMs in a similar fashion to the EHTs revealed that mavacamten treatment differentially decreased cell size of HCM iPSC-CMs (Fig. 7, G and H). It therefore appeared that excess peak twitch force in HCM EHTs is due to cellular hypertrophy rather than to a direct effect of E192K tropomyosin but that E192K drives this through thin filament dysregulation, leading to excess residual bridge activity that can be attenuated with a cardiac-specific myosin inhibitor.

Discussion

We have used several complementary approaches to study the causes of severe HCM in a specific patient carrying the E192K mutation in TPM1. This work featured a thorough biomechanical examination of iPSC-CMs from the patient achieved by forming these cells into EHTs. To our knowledge, these experiments constitute the first assessment of TPM1 mutant contractile behavior in human-derived EHT. Patient EHTs revealed striking, fourfold increases in both isometric twitch force and diastolic force along with slowed relaxation. These changes were highly reminiscent of the patient's clinical phenotype, which featured severe hypertrophy and diastolic dysfunction.

Initially, we assumed that biomechanical phenotypes in such young tissues formed from iPSC-CMs would reveal the direct, acute contractile consequences of mutant tropomyosin. Multiscale computational modeling and in vitro motility data ultimately suggested that there was a disconnect at the tissue level from these direct biophysical changes. The mutation was predicted to increase PF by just 30% based solely on the effects of E192K on tropomyosin stiffness, much less than the fourfold increase manifested in EHTs. Furthermore, the regulated in vitro motility data showed a decrease in thin filament Ca^{2+} sensitivity when E192K was introduced. When E192K effects on tropomyosin stiffness and blocked–closed state equilibrium were incorporated into the model, the mutation was actually predicted to substantially decrease peak twitch force. While we could not be completely certain that the in vitro biochemical assay reflected the function of the excessive flexibility in the heterogenous myofilament, the evidence overall suggested that mutant TPM1 led to thin filament dysregulation and residual crossbridge activity.

We therefore considered the possibility that iPSC-CMs from the patient were already exhibiting hypertrophic growth, even at the early time points we used, as upregulation of hypertrophic signaling pathways in HCM CMs has been reported even in the absence of extrinsic mechanical and biochemical stressors (Davis et al., 2016). The dramatic enhancement of measured twitch force could simply be due to greater myofibrillar content in patient cells, which is expected with cellular hypertrophy. Indeed, patient-derived CMs showed significantly larger cell size and upregulation of the hypertrophic marker BNP.

We wondered how E192K might trigger cellular hypertrophy so potently. Although the modeling predicted reduction in active contractile force during systole, we noticed a small, but persistent presence of residual crossbridge activity when mutation effects were applied to the model. We hypothesized that this excess residual crossbridge activity could eventually drive hypertrophy. We showed in further EHT experiments that EHTs treated with the β-myosin heavy chain inhibitor mavacamten reduced systolic and even diastolic force with acute treatment, suggesting that residual crossbridge activity caused elevation in force during diastole. Using a chronic treatment, we found that mavacamten produced a robust elimination of the large difference in active contractile strength previously observed between patient and control EHT. Equalization of twitch force between the groups was not due to acute effects of mavacamten since tissues were characterized after 24 h of washout. Instead, the effect is likely mediated by normalization of myofibrillar content, as evidenced in decreased cell size and hypertrophic biomarkers with mavacamten treatment.

Ultimately, the accumulated observations and analysis lead us to conclude that TPM1 E192K provokes hypertrophic growth in CMs through excess residual crossbridge activity, particularly during diastole. Evidence for diastolic crossbridge activity in myofilaments with HCM sarcomeric variants has been noted previously in some studies. Early work by Kawai, Bai, and colleagues on HCM TPM1 variants used a protein-exchange system to replace WT animal protein in skinned fibers with that of recombinant mutant proteins for classic HCM variants, such as TPM1 E180G, D175N, and V95A (Bai et al., 2011). Mechanical measurements, including elegant sinusoidal perturbation analysis, on these filament systems revealed different functional effects depending on the variant but with an underlying factor of excess crossbridge activity at diastolic calcium levels, suggesting an underlying mechanism common to these HCM mutations in TPM1 (Bai et al., 2013).

More recently, Cammarato and colleagues studied important residues for TPM1–actin interactions in the thin filament, showing that HCM-associated actin variant A295S perturbed important intermolecular interactions (Viswanathan et al., 2017). Using in silico tools, in vitro motility assays, and ultimately a *Drosophila melanogaster* model, they found that the HCM variant actin A295S leads to hypercontractility by increasing thin filament calcium sensitivity. In particular, mutant *Drosophila* heart tubes showed restrictive physiology with decreased systolic function, prolonged contractions, and substantially reduced baseline heart tube diameters, indicating diastolic dysfunction. However, similar to our experiments using mavacamten to reduce EHT diastolic force acutely, they showed that abrogation of calcium-dependent and calcium-independent crossbridge binding via EGTA and blebbistatin relaxed heart tube diastolic diameters to normal values (Viswanathan et al., 2017), revealing the importance of diastolic crossbridge function controlled by actin–tropomyosin interactions in HCM pathophysiology (Schmidt and Cammarato, 2020).

As far as we are aware, this study is the first to offer assessment of diastolic mechanical behavior in an iPSC-CM model of thin filament HCM. Indeed, characterization of diastolic properties is absent from most published literature investigating HCM in iPSC-CMs (Eschenhagen and Carrier, 2019). However, Hinson and colleagues reported some baseline diastolic force increase in thick filament variants in HCM using their microtissue assay with iPSC-CMs. The increase was attenuated by treatment with the nonspecific actomyosin inhibitor blebbistatin (Cohn et al., 2019). Given our evidence and that of others, it may be argued that the diastolic dysfunction prevalent in HCM (Spirito and Maron, 1990) is attributable at least in part to direct effects of the HCM variant on myofilament function. This specific biophysical property may be driving aspects of myocardial remodeling. While calcium changes have been observed in some HCM model systems and, in particular, cellular and animal models, it was not apparent in this study at the tissue level, consistent with other human EHT studies (Mosqueira et al., 2018; Cohn et al., 2019). Hence, the role of Ca^{2+}-based hypertrophic signaling pathways in HCM remains unclear but may play a role in some specific forms of the disease (Lehman et al., 2019; Flenner et al., 2017). Indeed, calcium blocker–based therapies for HCM have not seemed to have clinically significant effects on cardiac remodeling but may be commonly used for their negative inotropic effect (Ho et al., 2015; Spoladore et al., 2012).

The TPM1 variant E192K has been reported since 2003 in association with cardiomyopathy (Van Driest et al., 2003) and, more recently, has been identified in a relatively large number of cases for a rare variant in TPM1 in the Atlas of Cardiac Genetic Variation (Walsh et al., 2017). Recently, there was a change in the status of E192K from VUS to pathogenic/likely pathogenic in ClinVar driven by standard genetic segregation determined by the Laboratory for Molecular Medicine. However, the functional and structural consequences of E192K in causing disease had not been fully characterized. Two computational studies published recently noted that E192K could alter actin–TPM1 interactions (Orzechowski et al., 2014a; Zheng et al., 2016). Our computational work on E192K in the current study agrees, to a large extent, with these published studies and further shows that the loss of filamentous flexibility could contribute to its effects of macroscopic muscle function. The ability for E192K to affect TPM1–actin interactions as well as lead to distant changes in flexibility along the coiled coil of TPM1 despite being located well away from TPM1–actin consensus binding sites (Redwood and Robinson, 2013) reveals the deceptively complex relationship of TPM1 structure to thin filament function. Previous studies on the two most well-described TPM1 HCM variants, E180G and D175N, revealed that TPM1 missense mutants could lead to delocalized effects, such as destabilizing inactivation of the thin filament occurring at sites well away from the usual actin and myosin binding areas, and to enhanced diastolic crossbridge cycling (Ly and Lehrer, 2012) and increased calcium sensitivity without severe overt changes to overall TPM1 structure (Chang et al., 2014), as explained in part by the substantial effect of these variants on TPM1 global and local flexibility (Li et al., 2012; Loong et al., 2012). Previous work has used MD and regulated in vitro motility to look at the HCM mutant E62Q (Farman et al., 2018). Similar to our results, that study concluded that considerations of flexibility and concomitant residue-specific alterations in interactions between actin and tropomyosin could indeed provide an explanation for altered thin filament calcium sensitivity (Farman et al., 2018).

While E192K does not seem to fall into a general paradigm of HCM mutations in TPM1 leading to increased calcium sensitivity, molecular features such as increased flexibility and destabilization of thin filament blocked-to-closed transitions seem plausible to explain E192K's effects on diastolic crossbridge cycling and myofilament function given previous findings (Redwood and Robinson, 2013; Tardiff, 2011; Williams et al., 2016, 2018; Manning et al., 2011). We worked here on connecting some features common at the TPM1 molecular and ensemble level to the mechanical function of intact human EHTs and found these as likely contributing to some aspects of patient functional phenotype and upregulation of hypertrophic pathways. However, we remain limited in further dissecting the secondary compensatory mechanisms that may impact patient phenotype, such as asymmetric LV hypertrophy and fibrosis, important work (Tardiff, 2011) that remains to be pursued by future investigations.

While our work here provides evidence for excess residual crossbridge activity contributing to HCM pathophysiology, we also show that treatment with an inhibitor of sarcomere contractility, mavacamten, can directly lead to reduction of pathological hypertrophy and improvement of diastolic function. While mavacamten as a cardiac myosin-specific chemomechanical inhibitor (Kawas et al., 2017) has been shown to specifically attenuate HCM in mouse models of HCM myosin variants with a biophysical insult of hypercontractility (Green et al., 2016), it had not been specifically shown to improve HCM in any model with a tropomyosin variant. Our data suggest benefits of mavacamten, even in HCM patient populations without thick filament mutations, by leading to acute improvement of diastolic function as well as long-term structural remodeling by chronic treatment. Such mechanisms may lend insight into recent phase 3 trial results that showed dramatic improvement in LV outflow tract gradient with chronic mavacamten treatment in obstructive HCM (Jacoby et al., 2021). The ability of mavacamten to improve diastolic properties, such as relaxation kinetics and diastolic force, in our human EHT model also suggests mechanisms through which mavacamten will benefit HCM patients without substantial obstruction, potentially improving their diastolic function regardless of structural remodeling (Ho et al., 2020). While it was not clear that a small molecule explicitly targeting myosin would counteract effects of a thin filament mutation, our data suggest that aberrant crossbridge activity, whether directly caused by myosin or indirectly via the cooperative actin–tropomyosin–myosin system, can be attenuated by a myosin small-molecule inhibitor and result in therapeutic effects. Furthermore, we suggest that targeting this mechanism can result in beneficial remodeling of the CM in vitro, which seems congruent with recently published cardiac imaging data in humans (Saberi et al., 2020).

Our approach using multiscale computational and experimental investigations is not without limitations. The structure of EHTs differs somewhat from that of intact animal CM preparations, such as trabeculae used traditionally in the field of muscle mechanics. As such, the cellular component of these EHTs does not occupy the entire cross-sectional area of the engineered tissue, a limitation present in every type of EHT to date. As a consequence, it was not possible to use macroscopic EHT cross-sectional area as an indicator of hypertrophy. Furthermore, visualization of sarcomere length via techniques such as laser diffraction during muscle testing is not currently feasible in these preparations. However, the precise, consistent, reproducible nature of the EHT produced through an optimized engineered process allows determination of the culture length (typically 5% above slack length) and the length of maximum force (10% stretch above culture length) in a fashion that is reproducible compared with some of the variability within animal muscle and between different animals. We also note that although cross-sectional area varies somewhat within any given batch of EHTs, this has not been found to correlate with twitch force across many experiments and cell lines used with this technique. Ultimately, for us, the advantages of being able to use human iPSC-CMs in a system allowing precise mechanical measurements of EHTs outweighed these limitations. We also made use of robust cellular imaging to assess hypertrophy in 2-D cultured CMs as a means of remedying some of the shortcomings of EHTs.

An additional limitation of an approach that leverages a wide variety of techniques, including MD, in vitro biochemical assays, and EHTs, is the potential for contextual variation. The in vitro motility assay here showed loss of calcium sensitivity, the opposite expected for a hypercontractile phenotype that has been cited as the pathophysiological basis of many HCM mutants (Ferrantini et al., 2017; Lynn et al., 2018; Yotti et al., 2019). Given that the ability to extract myofibrils or measure calcium concentration in skinned EHTs remains technically challenging, we probed the effects of TPM1 E192K using the regulated in vitro motility assay performed with mixtures of purified proteins. The assumption is that the loss of calcium sensitivity observed in that assay reflects what occurs in EHTs expressing E192K. Laying aside the many other instances where HCM mutations seem to enhance myofilament calcium sensitivity, one could consider the teleogically sensible possibility that the hypertrophy we observed in cells and tissues was the result of compensation by cells to maintain some ideal contractile force set point. However, if that were the case, then making the CMs even more hypocontractile with chronic mavacamten treatment would be expected then to produce further hypertrophy. However, as is clearly shown in our EHT and cell experiments, mavacamten-induced hypocontractility actually produced a regression of hypertrophy. Hence, regardless of how accurately the regulated in vitro motility results reflect the in situ behavior of TPM1 E192K in iPSC-CMs, we conclude that this mutation triggers hypertrophy through an inability to completely restrict myosin activity, whether in systole, diastole, or both.

While the idea that hypercontractility or residual crossbridge activity can drive hypertrophy is somewhat counterintuitive at first, it is without support in the literature. Indeed, the most common form of cardiac hypertrophy is driven by increased afterload, which is known to be a primary driver of ventricular contractility (Sonnenblick and Downing, 1963). Such results are also consistent with the work of Davis et al. (2016) who conducted a broad study comparing multiple (cTnC) cardiomyopathy mutant mice with in vivo measurements and isolated CM measurements of calcium and unloaded shortening and found that the only predictive functional correlate of subsequent hypertrophy was the TTI, which was elevated (hypercontractile) in HCM mice. Finally, by contrast, dilated cardiomyopathy mutations, which occur most commonly in titin, have been shown to cause hypocontractile sarcomeres and are associated with atrophy of CMs rather than hypertrophy (Streckfuss-Bömeke et al., 2017; McNally et al., 2015; Yotti et al., 2019; Hinson et al., 2015; Chopra et al., 2018).

Future work is still required to explore the detailed biophysical mechanisms whereby sarcomeric hyperactivity causes CM hypertrophy, and this topic remains an active investigation. While mavacamten works directly on the sarcomeric dysfunction in this thin filament–driven disease through thick–thin filament cooperativity and synergism in cardiac contraction, it is unclear how this leads to hypertrophy, although mechanosensing and mitogen-activated protein kinase signaling likely play a role. No calcium changes were observed in this study, disallowing pursuit of calcium-mediated hypertrophy pathways, which have been explored often in single-cell studies, though less often observed in published tissue-level models of disease. Pursuit of such understanding of the hypertrophic pathways would require extensive transcriptomic and proteomic analysis, which will be the subject of future work with refined tools. However, in an actionable sense, it is of inherent interest that this drug works for attenuating hypertrophy in HCM even in mutations not in the thick filament, and as such, it may be clinically relevant to consider this approach regardless of the biological minutiae.

Acknowledgments

Henk L. Granzier served as editor.

We acknowledge the following sources of support: National Institutes of Health grants R01HL036153 to W. Lehman, R01HL123774 to J.R. Moore and W. Lehman, R01HL136590 to S.G. Campbell, and 1R01HL131940; U.S. Department of Defense grants 11959515, W81XWH1910557 to Y. Qyang, and W81XWH-20-1-0036 to J. Park; American Heart Association postdoctoral fellowship to A.W. Racca; P.D. Soros Fellowship for New Americans, National Institutes of Health, National Institute of General Medical Sciences, Medical Scientist Training Program grant T32GM007205; and American Heart Association predoctoral fellowship to L.R. Sewanan.

J. Schwan and S.G. Campbell have equity ownership in Propria LLC, which has licensed the EHT technology used in the research reported in this publication. This arrangement has been reviewed and approved by the Yale University Conflict of Interest Office. The authors declare no additional competing financial interests.

Author contributions: L.R. Sewanan, D.L. Jacoby, J.R. Moore, Y. Qyang, W. Lehman, and S.G. Campbell contributed to the study design. L.R. Sewanan, J. Park, M.J. Rynkiewicz, A.W. Racca, J. Schwan, and N. Papoutsidakis contributed to the data collection. L.R. Sewanan, J. Park, M.J. Rynkiewicz, and A.W. Racca performed the data analysis. All authors participated in writing and revising the manuscript.

Submitted: 24 April 2020
Revised: 14 June 2021
Accepted: 9 July 2021

References

Adzhubei, I.A., S. Schmidt, L. Peshkin, V.E. Ramensky, A. Gerasimova, P. Bork, A.S. Kondrashov, and S.R. Sunyaev. 2010. A method and server for predicting damaging missense mutations. *Nat. Methods.* 7:248–249. https://doi.org/10.1038/nmeth0410-248

Aksel, T., E. Choe Yu, S. Sutton, K.M. Ruppel, and J.A. Spudich. 2015. Ensemble force changes that result from human cardiac myosin mutations and a small-molecule effector. *Cell Rep.* 11:910–920. https://doi.org/10.1016/j.celrep.2015.04.006

Bai, F., A. Weis, A.K. Takeda, P.B. Chase, and M. Kawai. 2011. Enhanced active cross-bridges during diastole: molecular pathogenesis of tropomyosin's HCM mutations. *Biophys. J.* 100:1014–1023. https://doi.org/10.1016/j.bpj.2011.01.001

Bai, F., L. Wang, and M. Kawai. 2013. A study of tropomyosin's role in cardiac function and disease using thin-filament reconstituted myocardium. *J. Muscle Res. Cell Motil.* 34:295–310. https://doi.org/10.1007/s10974-013-9343-z

Brooks, B.R., C.L. Brooks III, A.D. Mackerell Jr., L. Nilsson, R.J. Petrella, B. Roux, Y. Won, G. Archontis, C. Bartels, S. Boresch, et al. 2009. CHARMM: the biomolecular simulation program. *J. Comput. Chem.* 30:1545–1614. https://doi.org/10.1002/jcc.21287

Broughton, K.M., J. Li, E. Sarmah, C.M. Warren, Y.H. Lin, M.P. Henze, V. Sanchez-Freire, R.J. Solaro, and B. Russell. 2016. A myosin activator improves actin assembly and sarcomere function of human-induced pluripotent stem cell-derived cardiomyocytes with a troponin T point mutation. *Am. J. Physiol. Heart Circ. Physiol.* 311:H107–H117. https://doi.org/10.1152/ajpheart.00162.2016

Campbell, S.G., F.V. Lionetti, K.S. Campbell, and A.D. McCulloch. 2010. Coupling of adjacent tropomyosins enhances cross-bridge-mediated cooperative activation in a markov model of the cardiac thin filament. *Biophys. J.* 98:2254–2264. https://doi.org/10.1016/j.bpj.2010.02.010

Chang, A.N., N.J. Greenfield, A. Singh, J.D. Potter, and J.R. Pinto. 2014. Structural and protein interaction effects of hypertrophic and dilated cardiomyopathic mutations in alpha-tropomyosin. *Front. Physiol.* 5:460. https://doi.org/10.3389/fphys.2014.00460

Choi, Y., G.E. Sims, S. Murphy, J.R. Miller, and A.P. Chan. 2012. Predicting the functional effect of amino acid substitutions and indels. *PLoS One.* 7: e46688. https://doi.org/10.1371/journal.pone.0046688

Chopra, A., M.L. Kutys, K. Zhang, W.J. Polacheck, C.C. Sheng, R.J. Luu, J. Eyckmans, J.T. Hinson, J.G. Seidman, C.E. Seidman, and C.S. Chen. 2018. Force generation via β-cardiac myosin, titin, and α-actinin drives cardiac sarcomere assembly from cell-matrix adhesions. *Dev. Cell.* 44: 87–96.e5. https://doi.org/10.1016/j.devcel.2017.12.012

Cohn, R., K. Thakar, A. Lowe, F.A. Ladha, A.M. Pettinato, R. Romano, E. Meredith, Y.S. Chen, K. Atamanuk, B.D. Huey, and J.T. Hinson. 2019. A contraction stress model of hypertrophic cardiomyopathy due to sarcomere mutations. *Stem Cell Reports.* 12:71–83. https://doi.org/10.1016/j.stemcr.2018.11.015

Coppini, R., C.Y. Ho, E. Ashley, S. Day, C. Ferrantini, F. Girolami, B. Tomberli, S. Bardi, F. Torricelli, F. Cecchi, et al. 2014. Clinical phenotype and outcome of hypertrophic cardiomyopathy associated with thin-filament gene mutations. *J. Am. Coll. Cardiol.* 64:2589–2600. https://doi.org/10.1016/j.jacc.2014.09.059

Dash, B.C., K. Levi, J. Schwan, J. Luo, O. Bartulos, H. Wu, C. Qiu, T. Yi, Y. Ren, S. Campbell, et al. 2016. Tissue-engineered vascular rings from human iPSC-derived smooth muscle cells. *Stem Cell Reports.* 7:19–28. https://doi.org/10.1016/j.stemcr.2016.05.004

Davis, J., L.C. Davis, R.N. Correll, C.A. Makarewich, J.A. Schwanekamp, F. Moussavi-Harami, D. Wang, A.J. York, H. Wu, S.R. Houser, et al. 2016. A tension-based model distinguishes hypertrophic versus dilated cardiomyopathy. *Cell.* 165:1147–1159. https://doi.org/10.1016/j.cell.2016.04.002

Doran, M.H., E. Pavadai, M.J. Rynkiewicz, J. Walklate, E. Bullitt, J.R. Moore, M. Regnier, M.A. Geeves, and W. Lehman. 2020. Cryo-EM and molecular docking shows myosin loop 4 contacts actin and tropomyosin on thin filaments. *Biophys. J.* 119:821–830. https://doi.org/10.1016/j.bpj.2020.07.006

Eschenhagen, T., and L. Carrier. 2019. Cardiomyopathy phenotypes in human-induced pluripotent stem cell-derived cardiomyocytes-a systematic review. *Pflugers Arch.* 471:755–768. https://doi.org/10.1007/s00424-018-2214-0

Farman, G.P., M.J. Rynkiewicz, M. Orzechowski, W. Lehman, and J.R. Moore. 2018. HCM and DCM cardiomyopathy-linked α-tropomyosin mutations influence off-state stability and crossbridge interaction on thin filaments. *Arch. Biochem. Biophys.* 647:84–92. https://doi.org/10.1016/j.abb.2018.04.002

Ferrantini, C., R. Coppini, J.M. Pioner, F. Gentile, B. Tosi, L. Mazzoni, B. Scellini, N. Piroddi, A. Laurino, L. Santini, et al. 2017. Pathogenesis of hypertrophic cardiomyopathy is mutation rather than disease specific: a comparison of the cardiac troponin T E163R and R92Q mouse models. *J. Am. Heart Assoc.* 6:e005407. https://doi.org/10.1161/JAHA.116.005407

Flenner, F., B. Geertz, S. Reischmann-Düsener, F. Weinberger, T. Eschenhagen, L. Carrier, and F.W. Friedrich. 2017. Diltiazem prevents stress-induced contractile deficits in cardiomyocytes, but does not reverse the cardiomyopathy phenotype in Mybpc3-knock-in mice. *J. Physiol.* 595:3987–3999. https://doi.org/10.1113/JP273769

Gersh, B.J., B.J. Maron, R.O. Bonow, J.A. Dearani, M.A. Fifer, M.S. Link, S.S. Naidu, R.A. Nishimura, S.R. Ommen, H. Rakowski, et al. American College of Cardiology Foundation/American Heart Association Task Force on Practice Guidelines. American Association for Thoracic Surgery. American Society of Echocardiography. American Society of Nuclear Cardiology. Heart Failure Society of America. Heart Rhythm Society. Society for Cardiovascular Angiography and Interventions. Society of Thoracic Surgeons. 2011. 2011 ACCF/AHA guideline for the diagnosis and treatment of hypertrophic cardiomyopathy: a report of the American College of Cardiology Foundation/American Heart Association Task Force on Practice Guidelines. *Circulation.* 124:e783–e831. https://doi.org/10.1161/CIR.0b013e318223e2bd

Green, E.M., H. Wakimoto, R.L. Anderson, M.J. Evanchik, J.M. Gorham, B.C. Harrison, M. Henze, R. Kawas, J.D. Oslob, H.M. Rodriguez, et al. 2016. A small-molecule inhibitor of sarcomere contractility suppresses hypertrophic cardiomyopathy in mice. *Science.* 351:617–621. https://doi.org/10.1126/science.aad3456

Hinson, J.T., A. Chopra, N. Nafissi, W.J. Polacheck, C.C. Benson, S. Swist, J. Gorham, L. Yang, S. Schafer, C.C. Sheng, et al. 2015. HEART DISEASE. Titin mutations in iPS cells define sarcomere insufficiency as a cause of dilated cardiomyopathy. *Science.* 349:982–986. https://doi.org/10.1126/science.aaa5458

Hirt, M.N., J. Boeddinghaus, A. Mitchell, S. Schaaf, C. Börnchen, C. Müller, H. Schulz, N. Hubner, J. Stenzig, A. Stoehr, et al. 2014. Functional improvement and maturation of rat and human engineered heart tissue by chronic electrical stimulation. *J. Mol. Cell. Cardiol.* 74:151–161. https://doi.org/10.1016/j.yjmcc.2014.05.009

Ho, C.Y., N.K. Lakdawala, A.L. Cirino, S.E. Lipshultz, E. Sparks, S.A. Abbasi, R.Y. Kwong, E.M. Antman, C. Semsarian, A. González, et al. 2015. Diltiazem treatment for pre-clinical hypertrophic cardiomyopathy sarcomere mutation carriers: a pilot randomized trial to modify disease expression. *JACC Heart Fail.* 3:180–188. https://doi.org/10.1016/j.jchf.2014.08.003

Ho, C.Y., M.E. Mealiffe, R.G. Bach, M. Bhattacharya, L. Choudhury, J.M. Edelberg, S.M. Hegde, D. Jacoby, N.K. Lakdawala, S.J. Lester, et al. 2020. Evaluation of mavacamten in symptomatic patients with nonobstructive hypertrophic cardiomyopathy. *J. Am. Coll. Cardiol.* 75:2649–2660. https://doi.org/10.1016/j.jacc.2020.03.064

Humphrey, J.D., R.K. Strumpf, and F.C.P. Yin. 1990. Determination of a constitutive relation for passive myocardium: I. A new functional form. *J. Biomech. Eng.* 112:333–339. https://doi.org/10.1115/1.2891193

Humphrey, W., A. Dalke, and K. Schulten. 1996. VMD: visual molecular dynamics. *J. Mol. Graph.* 14:33–38: 27–28. https://doi.org/10.1016/0263-7855(96)00018-5

Jacoby, D., C.Y. Ho, S.J. Lester, A. Wang, and I. Olivotto. 2021. Mavacamten for hypertrophic obstructive cardiomyopathy - Authors' reply. *Lancet.* 397: 369–370. https://doi.org/10.1016/S0140-6736(20)32391-6

Kawas, R.F., R.L. Anderson, S.R.B. Ingle, Y. Song, A.S. Sran, and H.M. Rodriguez. 2017. A small-molecule modulator of cardiac myosin acts on multiple stages of the myosin chemomechanical cycle. *J. Biol. Chem.* 292: 16571–16577. https://doi.org/10.1074/jbc.M117.776815

Kolanowski, T.J., C.L. Antos, and K. Guan. 2017. Making human cardiomyocytes up to date: Derivation, maturation state and perspectives. *Int. J. Cardiol.* 241:379–386. https://doi.org/10.1016/j.ijcard.2017.03.099

Land, S., and S.A. Niederer. 2015. A spatially detailed model of isometric contraction based on competitive binding of troponin I explains cooperative interactions between tropomyosin and crossbridges. *PLOS Comput. Biol.* 11:e1004376. https://doi.org/10.1371/journal.pcbi.1004376

Lehman, W., A. Galińska-Rakoczy, V. Hatch, L.S. Tobacman, and R. Craig. 2009. Structural basis for the activation of muscle contraction by troponin and tropomyosin. *J. Mol. Biol.* 388:673–681. https://doi.org/10.1016/j.jmb.2009.03.060

Lehman, S.J., L. Tal-Grinspan, M.L. Lynn, J. Strom, G.E. Benitez, M.E. Anderson, and J.C. Tardiff. 2019. Chronic calmodulin-kinase II activation drives disease progression in mutation-specific hypertrophic cardiomyopathy. *Circulation.* 139:1517–1529. https://doi.org/10.1161/CIRCULATIONAHA.118.034549

Lek, M., K.J. Karczewski, E.V. Minikel, K.E. Samocha, E. Banks, T. Fennell, A.H. O'Donnell-Luria, J.S. Ware, A.J. Hill, B.B. Cummings, et al. Exome Aggregation Consortium. 2016. Analysis of protein-coding genetic variation in 60,706 humans. *Nature.* 536:285–291. https://doi.org/10.1038/nature19057

Li, X.E., K.C. Holmes, W. Lehman, H. Jung, and S. Fischer. 2010a. The shape and flexibility of tropomyosin coiled coils: implications for actin filament assembly and regulation. *J. Mol. Biol.* 395:327–339. https://doi.org/10.1016/j.jmb.2009.10.060

Li, X.E., W. Lehman, and S. Fischer. 2010b. The relationship between curvature, flexibility and persistence length in the tropomyosin coiled-coil. *J. Struct. Biol.* 170:313–318. https://doi.org/10.1016/j.jsb.2010.01.016

Li, X.E., W. Suphamungmee, M. Janco, M.A. Geeves, S.B. Marston, S. Fischer, and W. Lehman. 2012. The flexibility of two tropomyosin mutants, D175N and E180G, that cause hypertrophic cardiomyopathy. *Biochem. Biophys. Res. Commun.* 424:493–496. https://doi.org/10.1016/j.bbrc.2012.06.141

Lian, X., J. Zhang, S.M. Azarin, K. Zhu, L.B. Hazeltine, X. Bao, C. Hsiao, T.J. Kamp, and S.P. Palecek. 2013. Directed cardiomyocyte differentiation from human pluripotent stem cells by modulating Wnt/β-catenin signaling under fully defined conditions. *Nat. Protoc.* 8:162–175. https://doi.org/10.1038/nprot.2012.150

Loong, C.K.P.P., H.-X.X. Zhou, and P.B. Chase. 2012. Familial hypertrophic cardiomyopathy related E180G mutation increases flexibility of human cardiac α-tropomyosin. *FEBS Lett.* 586:3503–3507. https://doi.org/10.1016/j.febslet.2012.08.005

Ly, S., and S.S. Lehrer. 2012. Long-range effects of familial hypertrophic cardiomyopathy mutations E180G and D175N on the properties of tropomyosin. *Biochemistry.* 51:6413–6420. https://doi.org/10.1021/bi3006835

Lynn, M.L., S.J. Lehman, and J.C. Tardiff. 2018. Biophysical derangements in genetic cardiomyopathies. *Heart Fail. Clin.* 14:147–159. https://doi.org/10.1016/j.hfc.2017.12.002

Manning, E.P., J.C. Tardiff, and S.D. Schwartz. 2011. A model of calcium activation of the cardiac thin filament. *Biochemistry.* 50:7405–7413. https://doi.org/10.1021/bi200506k

Margossian, S.S., and S. Lowey. 1982. Preparation of myosin and its subfragments from rabbit skeletal muscle. *Methods Enzymol.* 85(Pt B):55–71. https://doi.org/10.1016/0076-6879(82)85009-X

Marian, A.J., and E. Braunwald. 2017. Hypertrophic cardiomyopathy. *Circ. Res.* 121:749–770. https://doi.org/10.1161/CIRCRESAHA.117.311059

McNally, E.M., D.Y. Barefield, and M.J. Puckelwartz. 2015. The genetic landscape of cardiomyopathy and its role in heart failure. *Cell Metab.* 21: 174–182. https://doi.org/10.1016/j.cmet.2015.01.013

Mosqueira, D., I. Mannhardt, J.R. Bhagwan, K. Lis-Slimak, P. Katili, E. Scott, M. Hassan, M. Prondzynski, S.C. Harmer, A. Tinker, et al. 2018. CRISPR/Cas9 editing in human pluripotent stem cell-cardiomyocytes highlights arrhythmias, hypocontractility, and energy depletion as potential therapeutic targets for hypertrophic cardiomyopathy. *Eur. Heart J.* 39:3879–3892. https://doi.org/10.1093/eurheartj/ehy249

Mosqueira, D., J.G.W. Smith, J.R. Bhagwan, and C. Denning. 2019. Modeling hypertrophic cardiomyopathy: mechanistic insights and pharmacological intervention. *Trends Mol. Med.* 25:775–790. https://doi.org/10.1016/j.molmed.2019.06.005

Ng, R., L.R. Sewanan, P. Stankey, X. Li, Y. Qyang, and S. Campbell. 2020. Shortening velocity causes myosin isoform shift in human engineered heart tissues. *Circ. Res.* 128:281–283. https://doi.org/10.1161/CIRCRESAHA.120.316950

Ojala, M., C. Prajapati, R.P. Pölönen, K. Rajala, M. Pekkanen-Mattila, J. Rasku, K. Larsson, and K. Aalto-Setälä. 2016. Mutation-specific phenotypes in hiPSC-derived cardiomyocytes carrying either myosin-binding protein C or α-tropomyosin mutation for hypertrophic cardiomyopathy. *Stem Cells Int.* 2016:1684792. https://doi.org/10.1155/2016/1684792

Orzechowski, M., S. Fischer, J.R. Moore, W. Lehman, and G.P. Farman. 2014a. Energy landscapes reveal the myopathic effects of tropomyosin mutations. *Arch. Biochem. Biophys.* 564:89–99. https://doi.org/10.1016/j.abb.2014.09.007

Orzechowski, M., X.E. Li, S. Fischer, and W. Lehman. 2014b. An atomic model of the tropomyosin cable on F-actin. *Biophys. J.* 107:694–699. https://doi.org/10.1016/j.bpj.2014.06.034

Pavadai, E., W. Lehman, and M.J. Rynkiewicz. 2020. Protein-protein docking reveals dynamic interactions of tropomyosin on actin filaments. *Biophys. J.* 119:75–86. https://doi.org/10.1016/j.bpj.2020.05.017

Potter, J.D. 1982. Preparation of troponin and its subunits. *Methods Enzymol.* 85(Pt B):241–263. https://doi.org/10.1016/0076-6879(82)85024-6

Redwood, C., and P. Robinson. 2013. Alpha-tropomyosin mutations in inherited cardiomyopathies. *J. Muscle Res. Cell Motil.* 34:285–294. https://doi.org/10.1007/s10974-013-9358-5

Rynkiewicz, M.J., V. Schott, M. Orzechowski, W. Lehman, and S. Fischer. 2015. Electrostatic interaction map reveals a new binding position for tropomyosin on F-actin. *J. Muscle Res. Cell Motil.* 36:525–533. https://doi.org/10.1007/s10974-015-9419-z

Saberi, S., N. Cardim, M.H. Yamani, J. Schulz-Menger, W. Li, V. Florea, A.J. Sehnert, R.Y. Kwong, M. Jerosch-Herold, A. Masri, et al. 2020. Mavacamten favorably impacts cardiac structure in obstructive hypertrophic cardiomyopathy: EXPLORER-HCM CMR substudy analysis. *Circulation.* https://doi.org/10.1161/CIRCULATIONAHA.120.052359

Schmidt, W., and A. Cammarato. 2020. The actin 'A-triad's' role in contractile regulation in health and disease. *J. Physiol.* 598:2897–2908. https://doi.org/10.1113/JP276741

Schwan, J., and S.G. Campbell. 2015. Prospects for in vitro myofilament maturation in stem cell-derived cardiac myocytes. *Biomark. Insights.* 10(Suppl 1):91–103. https://doi.org/10.4137/BMI.S23912

Schwan, J., A.T. Kwaczala, T.J. Ryan, O. Bartulos, Y. Ren, L.R. Sewanan, A.H. Morris, D.L. Jacoby, Y. Qyang, and S.G. Campbell. 2016. Anisotropic engineered heart tissue made from laser-cut decellularized myocardium. *Sci. Rep.* 6:32068. https://doi.org/10.1038/srep32068

Seki, T., S. Yuasa, and K. Fukuda. 2012. Generation of induced pluripotent stem cells from a small amount of human peripheral blood using a combination of activated T cells and Sendai virus. *Nat. Protoc.* 7:718–728. https://doi.org/10.1038/nprot.2012.015

Sewanan, L.R., and S.G. Campbell. 2020. Modelling sarcomeric cardiomyopathies with human cardiomyocytes derived from induced pluripotent stem cells. *J. Physiol.* 598:2909–2922. https://doi.org/10.1113/JP276753

Sewanan, L.R., J.R. Moore, W. Lehman, and S.G. Campbell. 2016. Predicting effects of tropomyosin mutations on cardiac muscle contraction through myofilament modeling. *Front. Physiol.* 7:473. https://doi.org/10.3389/fphys.2016.00473

Sewanan, L.R., J. Schwan, J. Kluger, J. Park, D.L.D.L. Jacoby, Y. Qyang, and S.G.S.G. Campbell. 2019. Extracellular matrix from hypertrophic myocardium provokes impaired twitch dynamics in healthy cardiomyocytes. *JACC Basic Transl. Sci.* 4:495–505. https://doi.org/10.1016/j.jacbts.2019.03.004

Sewanan, L.R., S. Shen, and S.G. Campbell. 2021. Mavacamten preserves length-dependent contractility and improves diastolic function in human engineered heart tissue. *Am. J. Physiol. Heart Circ. Physiol.* 320: H1112–H1123. https://doi.org/10.1152/ajpheart.00325.2020

Shen, S., L.R. Sewanan, and S.G. Campbell. 2021. Evidence for synergy between sarcomeres and fibroblasts in an in vitro model of myocardial reverse remodeling. *J. Mol. Cell. Cardiol.* 158:11–25. https://doi.org/10.1016/j.yjmcc.2021.05.005

Sim, N.-L., P. Kumar, J. Hu, S. Henikoff, G. Schneider, and P.C. Ng. 2012. SIFT web server: predicting effects of amino acid substitutions on proteins. *Nucleic Acids Res.* 40(Web Server issue, W1):W452-7. https://doi.org/10.1093/nar/gks539

Sonnenblick, E.H., and S.E. Downing. 1963. Afterload as a primary determinat of ventricular performance. *Am. J. Physiol.* 204:604–610. https://doi.org/10.1152/ajplegacy.1963.204.4.604

Spirito, P., and B.J. Maron. 1990. Relation between extent of left ventricular hypertrophy and diastolic filling abnormalities in hypertrophic cardiomyopathy. *J. Am. Coll. Cardiol.* 15:808–813. https://doi.org/10.1016/0735-1097(90)90278-W

Spoladore, R., M.S. Maron, R. D'Amato, P.G. Camici, and I. Olivotto. 2012. Pharmacological treatment options for hypertrophic cardiomyopathy: high time for evidence. *Eur. Heart J.* 33:1724–1733. https://doi.org/10.1093/eurheartj/ehs150

Streckfuss-Bömeke, K., M. Tiburcy, A. Fomin, X. Luo, W. Li, C. Fischer, C. Özcelik, A. Perrot, S. Sossalla, J. Haas, et al. 2017. Severe DCM phenotype of patient harboring RBM20 mutation S635A can be modeled by patient-specific induced pluripotent stem cell-derived cardiomyocytes. *J. Mol. Cell. Cardiol.* 113:9–21. https://doi.org/10.1016/j.yjmcc.2017.09.008

Sun, N., M. Yazawa, J. Liu, L. Han, V. Sanchez-Freire, O.J. Abilez, E.G. Navarrete, S. Hu, L. Wang, A. Lee, et al. 2012. Patient-specific induced pluripotent stem cells as a model for familial dilated cardiomyopathy. *Sci. Transl. Med.* 4:130ra47. https://doi.org/10.1126/scitranslmed.3003552

Tardiff, J.C. 2005. Sarcomeric proteins and familial hypertrophic cardiomyopathy: linking mutations in structural proteins to complex cardiovascular phenotypes. *Heart Fail. Rev.* 10:237–248. https://doi.org/10.1007/s10741-005-5253-5

Tardiff, J.C. 2011. Thin filament mutations: developing an integrative approach to a complex disorder. *Circ. Res.* 108:765–782. https://doi.org/10.1161/CIRCRESAHA.110.224170

Van Driest, S.L., E.G. Ellsworth, S.R. Ommen, A.J. Tajik, B.J. Gersh, and M.J. Ackerman. 2003. Prevalence and spectrum of thin filament mutations in an outpatient referral population with hypertrophic cardiomyopathy. *Circulation.* 108:445–451. https://doi.org/10.1161/01.CIR.0000080896.52003.DF

Viswanathan, M.C., W. Schmidt, M.J. Rynkiewicz, K. Agarwal, J. Gao, J. Katz, W. Lehman, and A. Cammarato. 2017. Distortion of the actin a-triad results in contractile disinhibition and cardiomyopathy. *Cell Rep.* 20: 2612–2625. https://doi.org/10.1016/j.celrep.2017.08.070

Walsh, R., K.L. Thomson, J.S. Ware, B.H. Funke, J. Woodley, K.J. McGuire, F. Mazzarotto, E. Blair, A. Seller, J.C. Taylor, et al. Exome Aggregation Consortium. 2017. Reassessment of Mendelian gene pathogenicity using 7,855 cardiomyopathy cases and 60,706 reference samples. *Genet. Med.* 19:192–203. https://doi.org/10.1038/gim.2016.90

Wang, L., K. Kim, S. Parikh, A.G. Cadar, K.R. Bersell, H. He, J.R. Pinto, D.O. Kryshtal, and B.C. Knollmann. 2018. Hypertrophic cardiomyopathy-linked mutation in troponin T causes myofibrillar disarray and pro-arrhythmic action potential changes in human iPSC cardiomyocytes. *J. Mol. Cell. Cardiol.* 114:320–327. https://doi.org/10.1016/j.yjmcc.2017.12.002

Williams, M.R., S.J. Lehman, J.C. Tardiff, and S.D. Schwartz. 2016. Atomic resolution probe for allostery in the regulatory thin filament. *Proc. Natl. Acad. Sci. USA.* 113:3257–3262. https://doi.org/10.1073/pnas.1519541113

Williams, M.R., J.C. Tardiff, and S.D. Schwartz. 2018. Mechanism of cardiac tropomyosin transitions on filamentous actin as revealed by all-atom steered molecular dynamics simulations. *J. Phys. Chem. Lett.* 9:3301–3306. https://doi.org/10.1021/acs.jpclett.8b00958

Wu, H., H. Yang, J.-W. Rhee, J.Z. Zhang, C.K. Lam, K. Sallam, A.C.Y. Chang, N. Ma, J. Lee, H. Zhang, et al. 2019. Modelling diastolic dysfunction in induced pluripotent stem cell-derived cardiomyocytes from hypertrophic cardiomyopathy patients. *Eur. Heart J.* 40:3685–3695. https://doi.org/10.1093/eurheartj/ehz326

Yamada, Y., K. Namba, and T. Fujii. 2020. Cardiac muscle thin filament structures reveal calcium regulatory mechanism. *Nat. Commun.* 11:153. https://doi.org/10.1038/s41467-019-14008-1

Yotti, R., C.E. Seidman, and J.G. Seidman. 2019. Advances in the genetic basis and pathogenesis of sarcomere cardiomyopathies. *Annu. Rev. Genomics Hum. Genet.* 20:129–153. https://doi.org/10.1146/annurev-genom-083118-015306

Zheng, W., S.E. Hitchcock-DeGregori, and B. Barua. 2016. Investigating the effects of tropomyosin mutations on its flexibility and interactions with filamentous actin using molecular dynamics simulation. *J. Muscle Res. Cell Motil.* 37:131–147. https://doi.org/10.1007/s10974-016-9447-3

Supplemental material

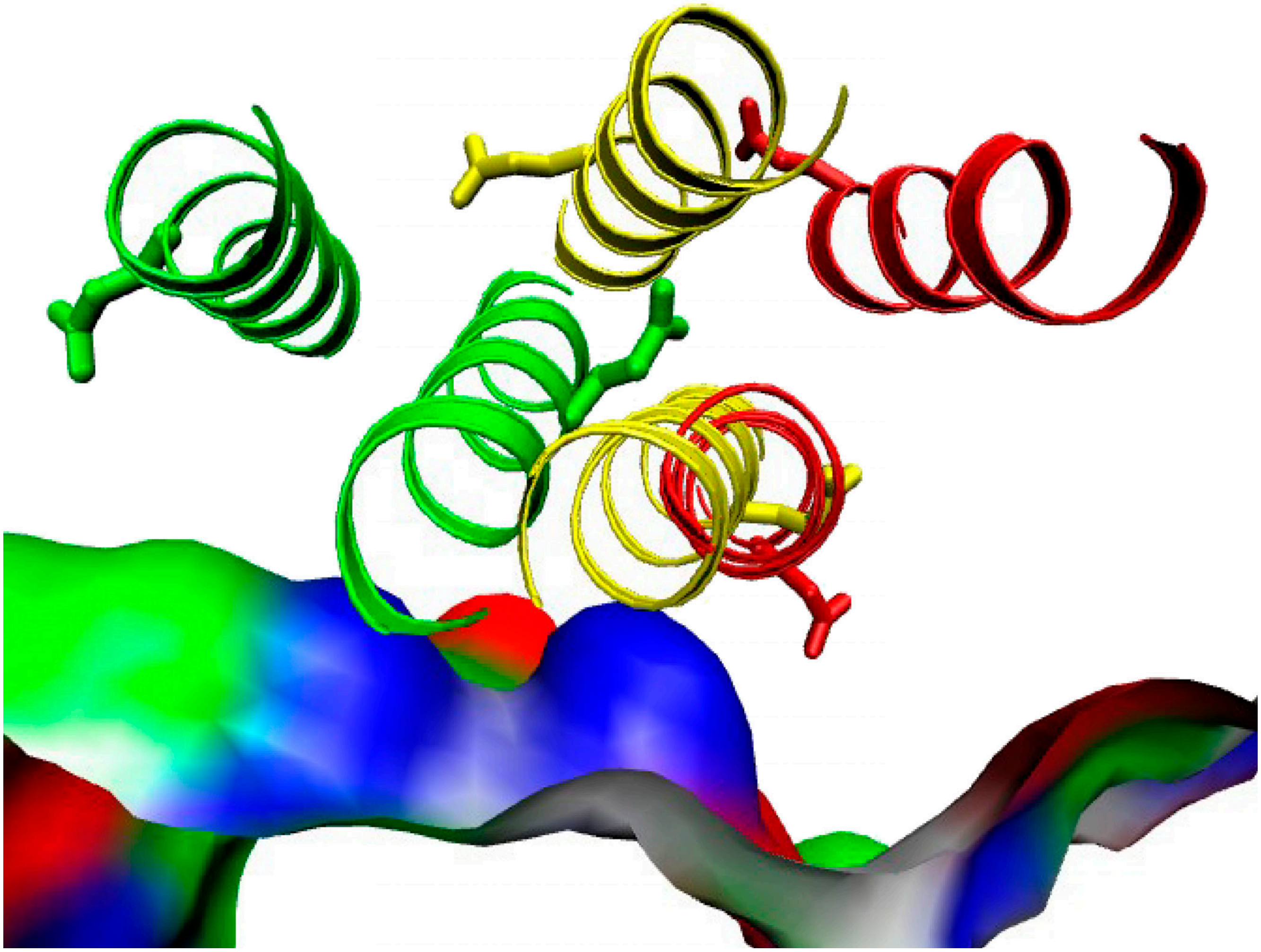

Figure S1. **Cryo-EM modeling of TPM1 traversing over actin.** E192 of tropomyosin moves across a positively charged surface on actin during regulatory transitions. Shown are ribbon diagrams of tropomyosin from the refined low Ca^{2+} (red) and high Ca^{2+} (green) cryo-EM structures (Yamada et al., 2020; Pavadai et al., 2020) and the cryo-EM structure of tropomyosin and actin saturated with cardiac myosin (green; Protein Data Bank accession no. 6X5Z; Doran et al., 2020). Actin is shown as a cutaway surface colored by residue type (blue for positively charged residues; red for negatively charged residues; green for polar, uncharged residues; and white for hydrophobic residues). Note that as E192 moves from the structural B state through the C state to the M state and back, it traverses a positive patch on actin formed by actin residues K215 and K238. Substitution of E192 with a lysine would be expected to create unfavorable interactions with this patch, thereby altering regulatory transitions, which in conjunction with altered persistence length would affect contraction and relaxation in mutant muscle.

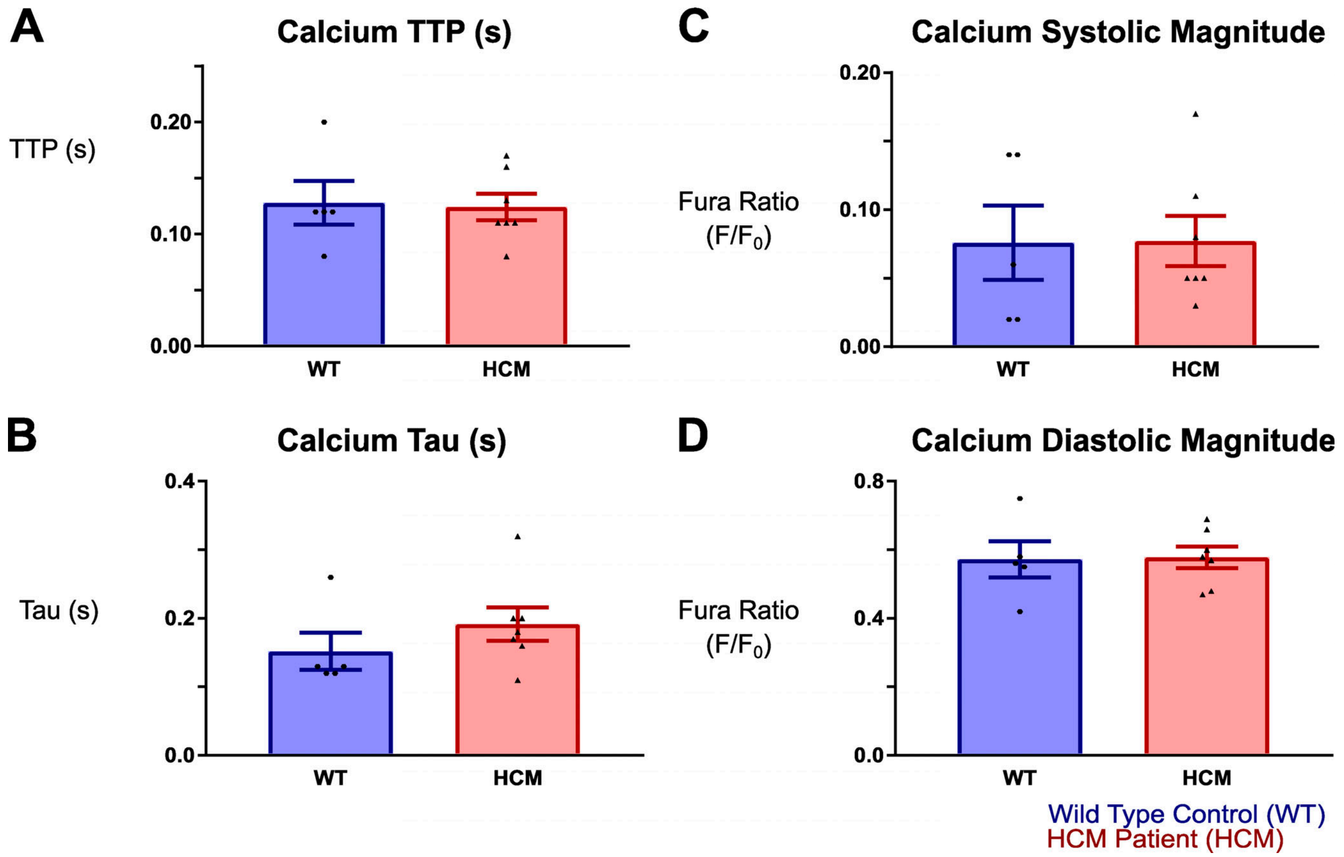

Figure S2. **Calcium transient measurements of EHTs made from WT and HCM iPSC-CMs. (A)** Calcium TTP was not significantly different between HCM and WT EHTs. **(B)** Calcium exponential decay constant from peak (Tau) was not significantly different between HCM and WT EHTs. **(C)** Calcium systolic magnitude peak change ratio was not significantly different between HCM and WT EHTs. **(D)** Calcium diastolic magnitude ratio was not significantly different between HCM and WT EHTs.

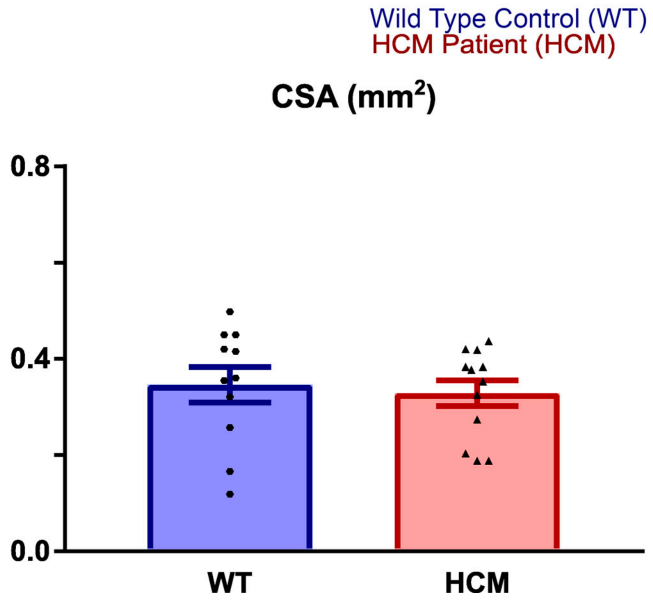

Figure S3. **Cross-sectional area (CSA) measurements of EHTs.** There was no difference in CSA of WT and HCM EHTs, which averaged ~0.34 mm^2.

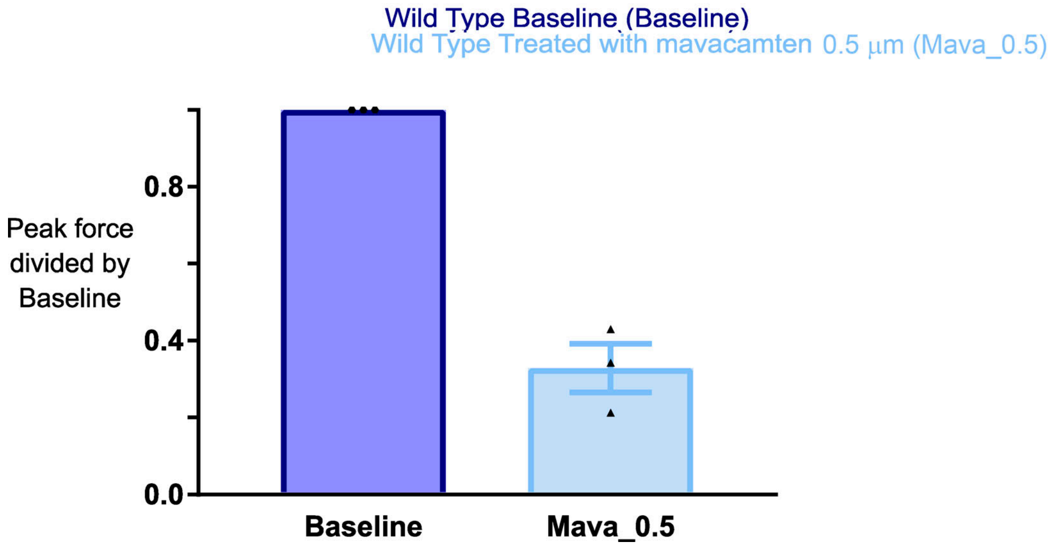

Figure S4. **Acute mavacamten treatment of WT EHTs.** Mavacamten treatment of WT EHTs resulted in an ~70% reduction in force produced at steady state at a concentration of 0.5 μM.